CM² MAGAZINE

第 79 期

南方科技大学海洋磁学中心主编

http://cm2.sustech.edu.cn/

创刊词

海洋是生命的摇篮，是文明的纽带。地球上最早的生命诞生于海洋，海洋里的生命最终进化成了人类，人类的文化融合又通过海洋得以实现。人因海而兴。

人类对海洋的探索从未停止。从远古时代美丽的神话传说，到麦哲伦的全球航行，再到现代对大洋的科学钻探计划，海洋逐渐从人类敬畏崇拜幻想的精神寄托演变成可以开发利用与科学研究的客观存在。其中，上个世纪与太空探索同步发展的大洋科学钻探计划将人类对海洋的认知推向了崭新的纬度：深海（deep sea）与深时（deep time）。大洋钻探计划让人类知道，奔流不息的大海之下，埋藏的却是亿万年的地球历史。它们记录了地球板块的运动，从而使板块构造学说得到证实；它们记录了地球环境的演变，从而让古海洋学方兴未艾。

在探索海洋的悠久历史中，从大航海时代的导航，到大洋钻探计划中不可或缺的磁性地层学，磁学发挥了不可替代的作用。这不是偶然，因为从微观到宏观，磁性是最基本的物理属性之一，可以说，万物皆有磁性。基于课题组的学科背景和对海洋的理解，我们对海洋的探索以磁学为主要手段，海洋磁学中心因此而生。

海洋磁学中心，简称 CM^2，一为其全名“Centre for Marine Magnetism”的缩写，另者恰与爱因斯坦著名的质能方程 $E = MC^2$ 对称，借以表达我们对科学巨匠的敬仰和对科学的不懈追求。

然而科学从来不是单打独斗的产物。我们以磁学为研究海洋的主攻利器，但绝不仅限于磁学。凡与磁学相关的领域均是我们关注的重点。为了跟踪反映国内外地球科学特别是与磁学有关的地球科学领域的最新研究进展，海洋磁学中心特地主办 CM^2 Magazine，以期与各位地球科学工作者相互交流学习、合作共进！

“海洋孕育了生命，联通了世界，促进了发展”。 21 世纪是海洋科学的时代，由陆向海，让我们携手迈进中国海洋科学的黄金时代。

目录

一、研究进展

1. 晚中新世柴达木盆地千年分辨率降水变化及高低纬驱动研究

古气候 10 万年周期一般被认为与北半球冰盖的驱动有关。与 10 万年周期类似，古气候千年尺度波动的驱动力也被认为与北半球冰量千年尺度变化所导致的热盐环流的变化有关。然而少部分气候模拟实验表明，即使没有冰盖的驱动，大气、海洋和碳循环的耦合过程也可以产生 10 万年周期。针对北半球冰盖出现以前的古气候记录进行周期分析能够加深对 10 万年和千年尺度古气候变化机制的认识，然而目前那样的记录分辨率较低。

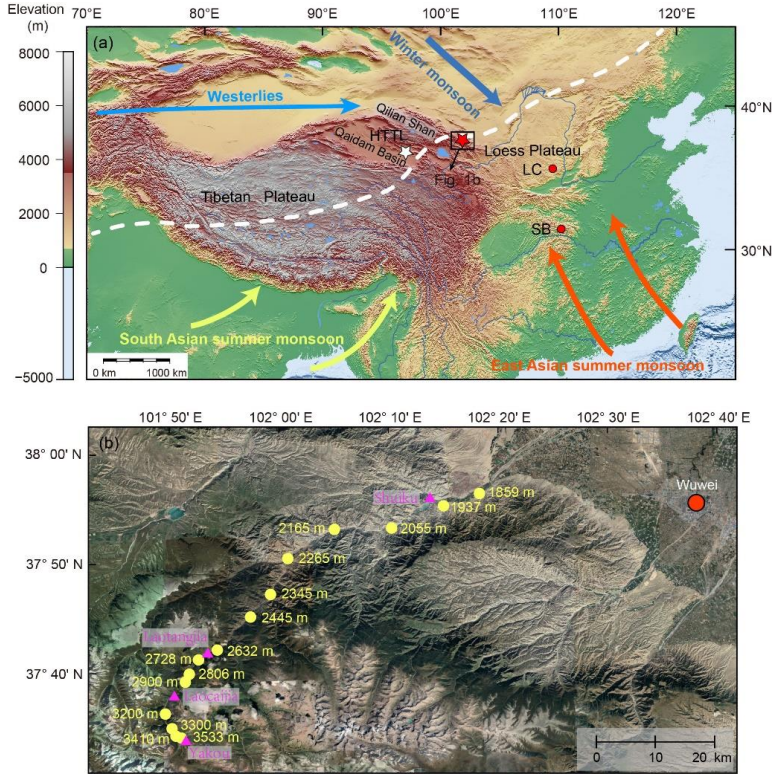

图 1. 采样点所在位置和现代大气环流模式图。（a）白色星号代表怀头他拉剖面 （HTTL），红色星号代表表土采样点位置，红色点代表收集数据的站点位置（LC: 洛川, SB: 三宝），白色虚线代表现代季风界限（Chen et al., 2010）；（b）黄色点代表表土采样点位置，数字表示海拔高度，紫色三角形代表气象站点。

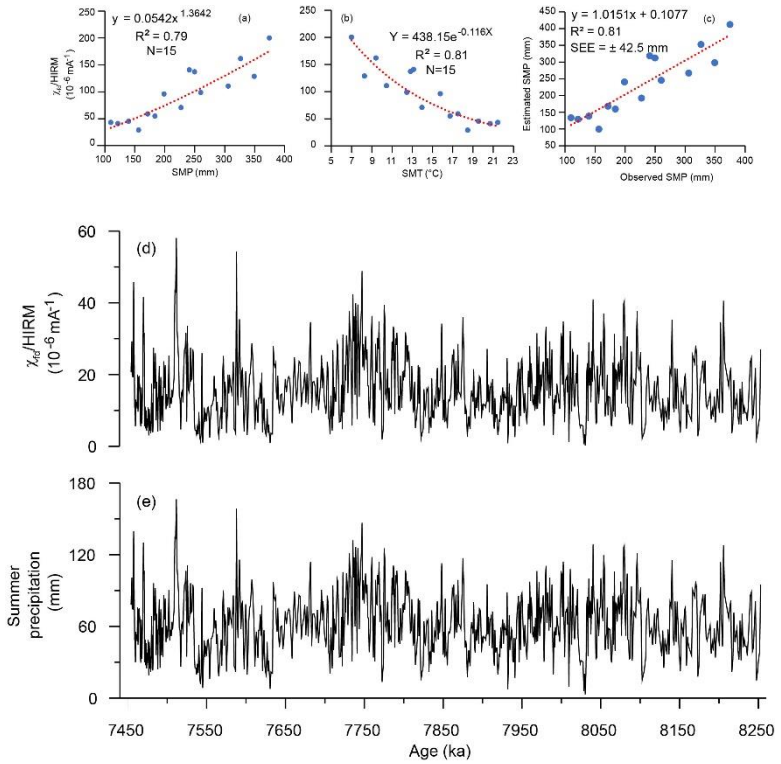

图 2. 定量重建晚中新世柴达木盆地怀头他拉剖面夏季降水。（a）χ_{fd}/HIRM 与夏季平均降水（SMP）之间的关系；（b）χ_{fd} /HIRM 与夏季平均气温（SMT）之间的关系；（c）实测降水与估算降水，SEE 代表标准误差；（d）晚中新世怀头他拉剖面时间序列上的 χ_{fd} /HIRM 变化；（e）定量重建的晚中新世怀头他拉剖面时间序列上的夏季平均降水变化。

为此，本研究选取柴达木盆地怀头他拉剖面（图 1）晚中新世的湖相沉积物开展了千年分辨率的古降水重建工作。基于高分辨率的古地磁年代模型，选用 χ_{fd} /HIRM 作为古降水代用指标，通过祁连山（图 1）现代表层土壤的 χ_{fd} /HIRM 与夏季平均降水之间的关系（图 2），定量获取了晚中新世怀头他拉剖面千年分辨率的古降水记录（图 2），年代跨度为 80 万年。

本研究获得了以下四点认识：

1. 祁连山表土的 χ_{fd}/HIRM 与降水成正比，而与温度（air temperature）变化成反比（图 2），这与黄土高原表土 χ_{fd}/HIRM 与温度和降水均呈现正相关不同。综合两地结果表明该指标主要受控于降水变化，而非温度。

2. 在所研究的大部分时间内，轨道时间尺度柴达木降水的变化主要受控于太阳辐射，这与石笋记录的东亚夏季风变化模式相符（图 3，4），说明柴达木盆

地降水可能来自于东亚季风降水。我们开展的初步气候模拟实验支持这一说法（图 5）。

3. 晚中新世柴达木降水存在显著的 10 万年周期，然而，在与未来轨道状况类似的低偏心率时期（8.13-8.03 Ma），柴达木降水的 10 万年周期并未减弱，与晚第四纪 MIS 11 阶段的情况类似（图 3）。值得注意的是，MIS 11 阶段北半球高纬度冰量的变化很大，10 万年周期的出现被归因为高纬度驱动的结果（图 3）。然而，8.13-8.03 Ma 期间高纬度冰量较小（图 4）。由此我们推断，8.13-8.03 Ma 期间较强的“100 kyr”周期的出现可能支持了 10 万年周期起源于地球气候系统内部的自由振荡的假说，说明冰量不是 10 万年周期变化的唯一驱动力。

4. 晚中新世柴达木降水存在显著的千年周期变化，且千年尺度变化的振幅强度与太阳辐射的小波相干性分析表明二者在 2 万、4 万和 10 万年尺度上具有显著的相关性（图 6），这可能支持了太阳辐射变化直接驱动千年尺度气候波动的假说。

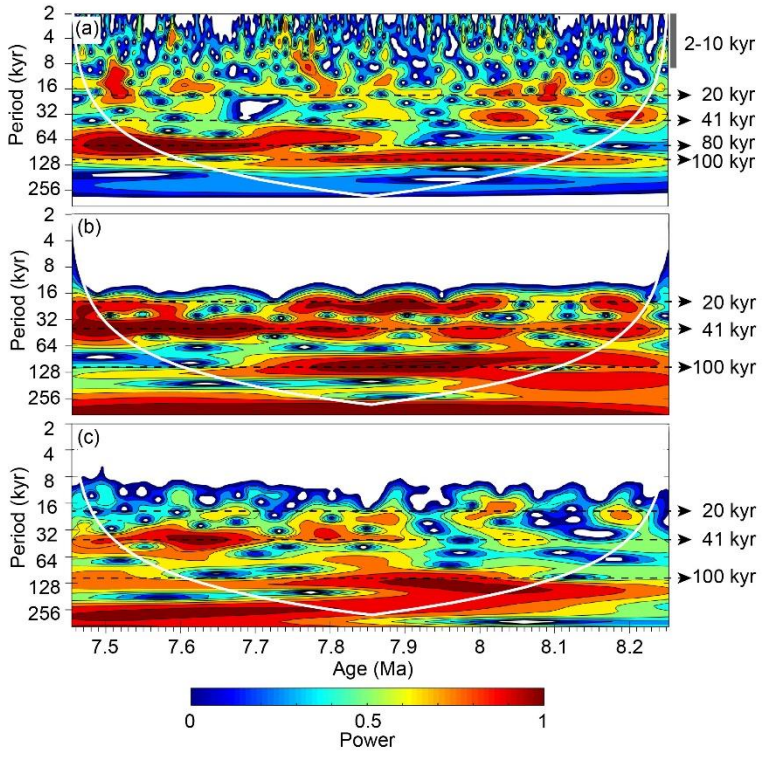

图 3. 小波分析结果。（a）怀头他拉剖面夏季平均降水；（b）ETP（偏心率—斜率—岁差）曲线（Laskar et al., 2004）；（c）深海氧同位素（Westerhold et al., 2020）。

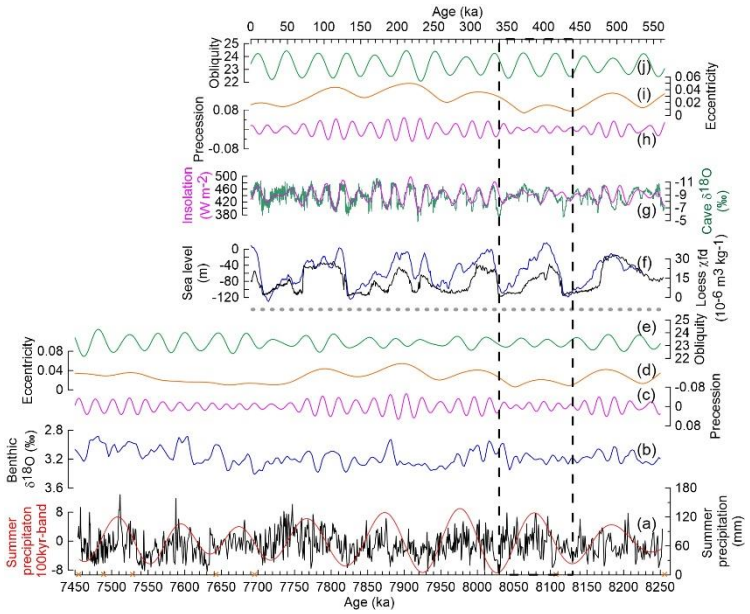

图 4. 晚中新世和晚第四纪期间中国北部降水记录与太阳辐射和冰量变化对比。（a）柴达木盆地怀头他拉剖面夏季平均降水记录（黑线）及其 100-kyr 周期滤波曲线（红线），x 轴上的黄色点代表 7 个地磁极性倒转的年龄锚点；（b）深海氧同位素（Westerhold et al., 2020）。（c-e）晚中新世的地球轨道岁差、偏心率和斜率曲线（Laskar et al., 2004）；（f）晚第四纪海平面变化（蓝线）（Spratt & Lisiecki, 2016）和洛川黄土频率磁化率（χ_{fd}）记录（黑线）（Hao et al., 2012）；（g）石笋氧同位素记录（绿线）和 6 月 21 日 65°N（粉线）太阳辐射变化曲线（Laskar et al., 2004）；（h-j）晚第四纪地球轨道岁差、偏心率和斜率曲线（Laskar et al., 2004）。

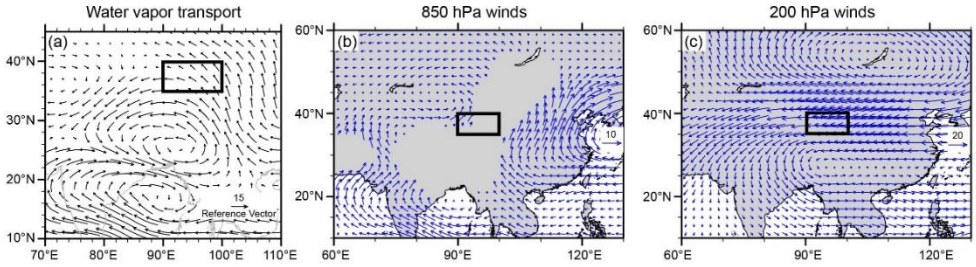

图 5. 气候模拟结果。（a）整层垂直水汽运输（kg m s^{-1}）及其辐散度(×10^{-6} kg m2 s^{-1})的差值场；晚中新世和工业革命前（b）850 hPa 和（c）200 hPa 风的差值场（m s^{-1}）。黑色矩形代表柴达木盆地。

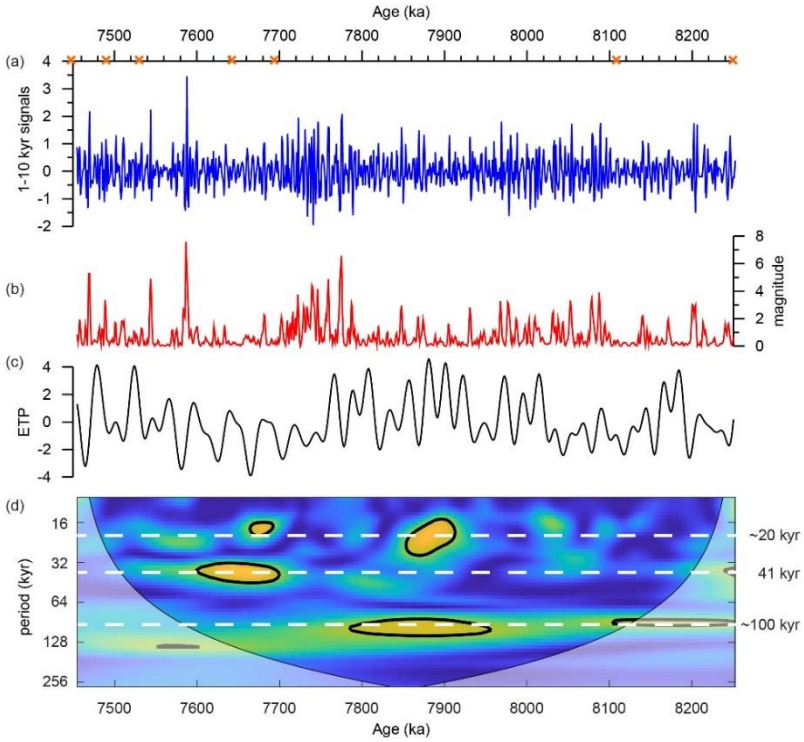

图 6. 晚中新世怀头他拉剖面夏季平均降水记录中的千年尺度气候波动。（a）1-10 kyr 周期信号；（b）1-10 kyr 周期信号的振幅；（c）ETP（偏心率—斜率—岁差）曲线（Laskar et al., 2004）；（d）1-10 kyr 周期信号的振幅与 ETP 的小波相干分析，x 轴上黄色点代表 7 个地磁极性倒转的年龄锚点。

本研究为理解晚中新世轨道和千年时间尺度上周期的起源提供了高分辨率的古环境记录，成果发表在《Geophysical Research Letters》。兰州大学西部环境教育部重点实验室博士生高鹏为本文的第一作者，兰州大学西部环境教育部重点实验室聂军胜教授、张旭教授和潘保田教授为本文的共同通讯作者。论文的其他合作者包括南方科技大学海洋科学与工程系刘青松讲席教授，中国科学院大气物理研究所燕青研究员，兰州大学西部环境教育部重点实验室曹泊副教授。本研究受第二次青藏高原综合科学考察课题（2019QZKK0704）资助。

论文链接：

Gao, P., Nie, J.*, Yan, Q., Zhang, X.*, Liu, Q., Cao, B., & Pan, B.* (2021). **Millennial resolution late Miocene northern China precipitation record spanning astronomical analogue interval to the future**. Geophysical Research Letters, 48, e2021GL093942. https://doi.org/10.1029/2021GL093942

二、文献速递

1. 过去两个间冰期间冰盖融化驱动北极甲烷气体释放

翻译人：仲义 zhongy@sustech.edu.cn

Dessandier P A, Knies J, Plaza-Faverola A, et al. ***Ice-sheet melt drove methane emissions in the Arctic during the last two interglacials****[J] Geology, 2021, 49(7), 799-803.*

https://doi.org/10.1130/G48580.1

摘要：环北极冰川正在以前所未有的方式融化，目前随着全球气候不断变暖，被封存的地质甲烷气体的释放可能会对全球冰盖的消退起到正反馈作用。而来自于冰期海冰更少，温度比现今更高的倒数第二个间冰期（距今 125 ka，Eemian）时期的甲烷释放的证据还很缺乏。本文，作者根据挪威维斯瓦尔巴特群岛近海钻孔的有孔虫同位素研究发现，在最后一次和倒数第二次冰期结束时，欧亚大陆冰盖的突然消融导致了甲烷气体的泄露。甲烷排放量的增加似乎首先是通过底栖有孔虫的 $\delta^{13}C$ 的降低所体现。其次，有孔虫壳体内外大量生长的自生碳酸盐表现出 $\delta^{18}O$ 偏重，贫 $\delta^{13}C$。在两次气候终止期出现的相似事件都支持了一个共同的驱动因素，即地质甲烷储量的周期性释放。作者的模型结果表明维斯瓦尔群岛西部边缘天然气水合物稳定带下方的浅层气藏的周期性泄露会在海底冰盖不稳定时期重新被激活。与这个模型类似的是，随着目前格陵兰岛冰融化的加速，冰盖下方和附近现有的甲烷储层很可能会更加不稳定。

ABSTRACT: Circum-Arctic glacial ice is melting in an unprecedented mode, and release of currently trapped geological methane may act as a positive feedback on ice-sheet retreat during global warming. Evidence for methane release during the penultimate (Eemian, ca. 125 ka) interglacial, a period with less glacial sea ice and higher temperatures than today, is currently absent. Here, we argue that based on foraminiferal isotope studies on drill holes from offshore Svalbard, Norway, methane

leakage occurred upon the abrupt Eurasian ice-sheet wastage during terminations of the last (Weichselian) and penultimate (Saalian) glaciations. Progressive increase of methane emissions seems to be first recorded by depleted benthic foraminiferal $\delta^{13}C$. This is quickly followed by the precipitation of methane-derived authigenic carbonate as overgrowth inside and outside foraminiferal shells, characterized by heavy $\delta^{18}O$ and depleted $\delta^{13}C$ of both benthic and planktonic foraminifera. The similarities between the events observed over both terminations advocate for a common driver for the episodic release of geological methane stocks. Our favored model is recurrent leakage of shallow gas reservoirs below the gas hydrate stability zone along the margin of western Svalbard that can be reactivated upon initial instability of the grounded, marine-based ice sheets. Analogous to this model, with the current acceleration of the Greenland ice melt, instabilities of existing methane reservoirs below and nearby the ice sheet are likely.

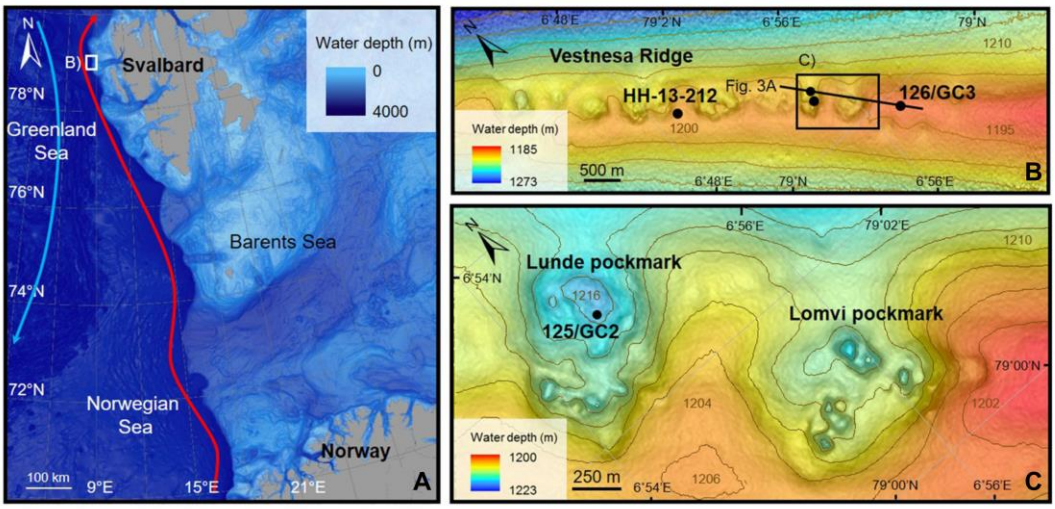

Figure 1. (A) Location map of Vestnesa Ridge, offshore Svalbard, Norway, where red arrow shows the North Atlantic Current, and blue arrow shows the East Greenland Current. (B) Pockmarks, cores, and seismic line used for chronostratigraphic correlation. (C) Location of studied core.

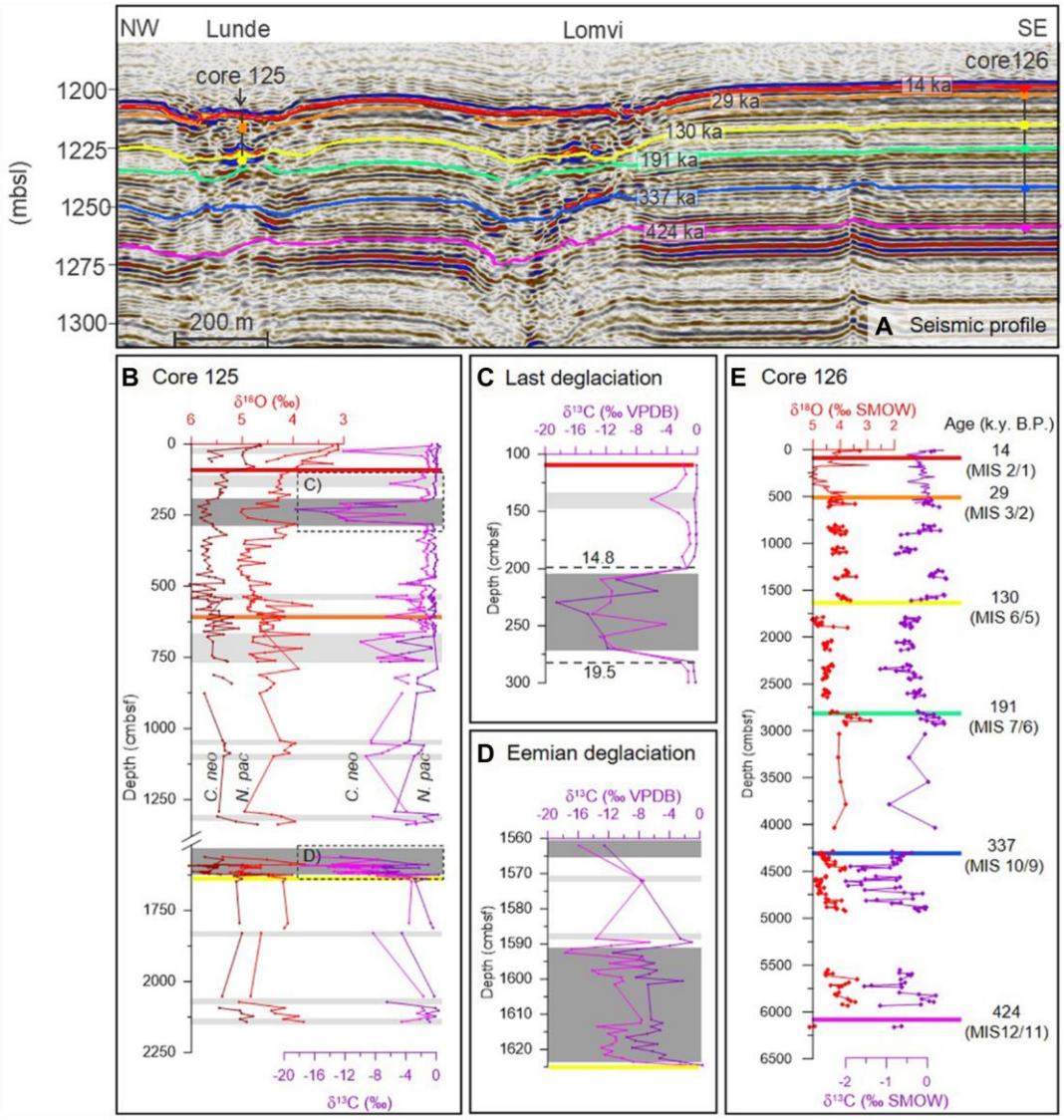

Figure 2. (A) Seismic profile showing continuation of reflections between the reference site MeBo126 and site MeBo125, Svalbard, Norway. mbsl - m below sea level. (B) Benthic (*C. neo* - *Cassidulina neoteretis*) and planktonic (*N. pac* - *N. Neogloboquadrina pachyderma*) foraminiferal stable isotopes of cores MeBo125 and GC2 (cmbsf - cm below seafloor). (C) Closeup of last deglaciation. VPDB - Vienna Peedeebelemnite. (D) Close-up of major seepage event over the Eemian interglacial from the record of core MeBo125. (E) Planktonic foraminiferal (*N. pachyderma*) stable isotopes of cores MeBo126 and GC3. SMOW - standard mean ocean water. Seismic profile is the transect from inline 133 in the three-dimensional seismic volume used by Plaza - Faverola et al. (2015). Seismic data were converted to depth using P-wave velocity information from Goswami et al. (2017) and Singhroha et al. (2019). MIS - marine isotope stage.

2. 通过晶体内同位素分析揭示 Sunda 弧地幔源区的 $\delta^{18}O$ 值

翻译人：冯婉仪 fengwy@sustech.edu.cn

Deegan F M, Whitehouse M J, Troll V R, et al. ***Sunda arc mantle source $\delta^{18}O$ value revealed by intracrystal isotope analysis****[J]. Nature Communications, 2021, 12:3930.*

https://doi.org/10.1038/s41467-021-24143-3

摘要：俯冲带火山下的岩浆通道系统从地幔延伸至上覆地壳，促进了岩浆长时间的分离结晶、同化和混合，这往往掩盖了地幔源区组成的真实情况。为了降低地壳内岩浆作用的影响，我们研究了来自印尼 Sunda 弧中 Merapi、Kelut、Batur 以及 Agung 火山的单斜辉石晶内二次离子质谱（SIMS）$\delta^{18}O$ 值，其中地壳厚度从 Merapi 火山的~ 30 km 减少至 Agung 火山的≤ 20 km。结果表明，单斜辉石平均 $\delta^{18}O$ 值随地壳厚度的增大而减小，并且 Agung 火山熔岩具有类似地幔的 He-Sr-Nd-Pb 同位素比值，其中与单斜辉石平衡的熔体的平均 $\delta^{18}O$ 值为 5.7‰（± 0.2 1SD），与大洋中脊玄武岩（MORB）的 $\delta^{18}O$ 值没有明显区别。东 Sunda 弧下地幔氧同位素组成基本不受俯冲交代作用的影响，因此，它可能代表了一个贫沉积物的弧端元。

ABSTRACT: Magma plumbing systems underlying subduction zone volcanoes extend from the mantle through the overlying crust and facilitate protracted fractional crystallisation, assimilation, and mixing, which frequently obscures a clear view of mantle source compositions. In order to see through this crustal noise, we present intracrystal Secondary Ion Mass Spectrometry (SIMS) $\delta^{18}O$ values in clinopyroxene from Merapi, Kelut, Batur, and Agung volcanoes in the Sunda arc, Indonesia, under which the thickness of the crust decreases from ca. 30 km at Merapi to ≤ 20 km at Agung. Here we show that mean clinopyroxene $\delta^{18}O$ values decrease concomitantly with crustal thickness and that lavas from Agung possess mantle-like He-Sr-Nd-Pb isotope ratios and clinopyroxene mean equilibrium melt $\delta^{18}O$ values of 5.7 ‰ (± 0.2 1SD) indistinguishable from the $\delta^{18}O$ range for Mid Ocean Ridge Basalt (MORB). The

oxygen isotope composition of the mantle underlying the East Sunda Arc is therefore largely unaffected by subduction-driven metasomatism and may thus represent a sediment-poor arc end-member.

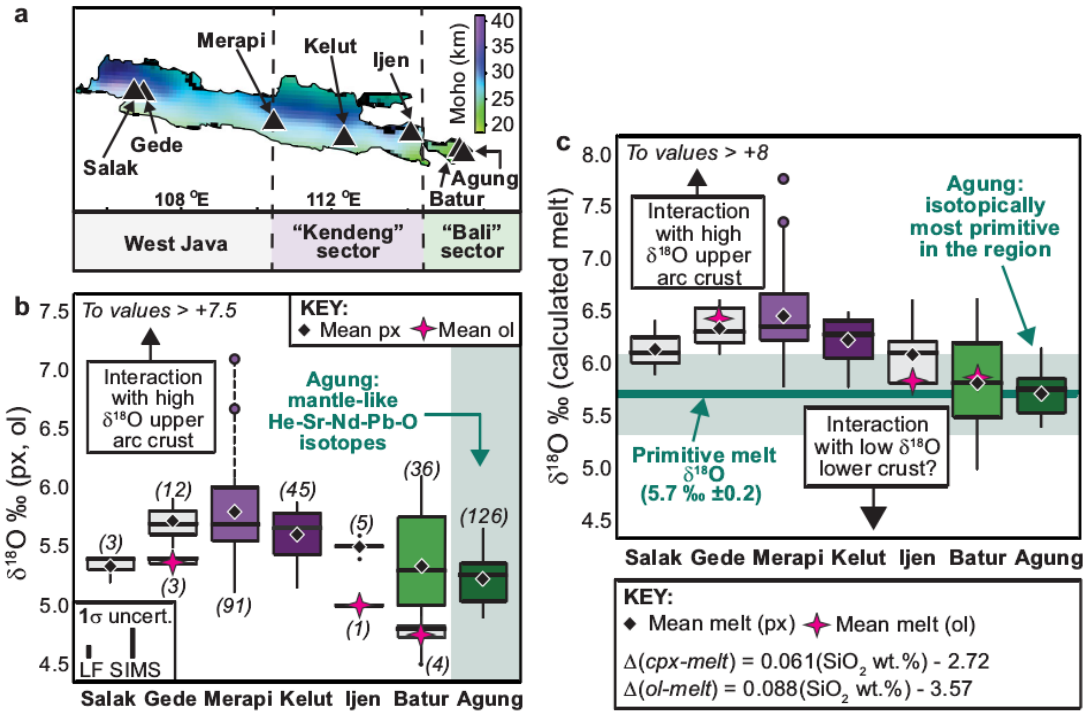

Figure 1. Arc-wide compilation of $\delta^{18}O$ values in mafic minerals and equilibrium melts. a Map of Java and Bali showing Moho depths estimated from Bouguer gravity anomalies (after ref. 40). The Moho lies at ca. 18-20 km beneath Bali compared to ca. 25-30 km beneath Central to East Java. b Box-and-whisker plots of pyroxene and olivine $\delta^{18}O$ values from volcanoes along the Java-Bali segment of the Sunda arc, showing grain averaged SIMS clinopyroxene data for Merapi, Kelut, Batur, and Agung (dark grey), pyroxene LF data for Salak[36], Gede[30], and Ijen[37], and olivine LF data for Gede[30], Ijen[37], and Batur (ref. 14 and this study). The number of analyses per volcano are given in parentheses. c Box-and-whisker plots of equilibrium melt $\delta^{18}O$ values calculated for the mineral data shown in panel b by employing the silica-dependent fractionation formulations of ref. 24. The clinopyroxene data suggest a parental melt $\delta^{18}O$ value of 5.7 ‰ (± 0.2 1SD for the Sunda arc. For most Javanese volcanoes, magmas are stored in the arc crust where they evolve while assimilating crustal materials, resulting in variably elevated $\delta^{18}O$ values in clinopyroxene. Data plotting was performed using the "ggplot2" package available via CRAN (Comprehensive R Archive Network; https://cran.r-project.org/). Abbreviations: cpx, clinopyroxene; ol, olivine; px, pyroxene).

3. 液态 Fe-8.5 wt% Si 到 24 GPa 的电阻率测量获得水星核的绝热热流

翻译人:李园洁 liyj3@sustech.edu.cn

Berrada M, Secco R A, Yong W. ***Adiabatic heat flow in Mercury's core from electrical resistivity measurements of liquid Fe-8.5 wt% Si to 24 GPa****[J]. Earth and Planetary Science Letters, 2021, 568, 117053.*

https://doi.org/10.1016/j.epsl.2021.117053

摘要：本文在压力 5-24 GPa，温度高于熔融温度时直接测量 Fe8.5Si 的电阻率来研究水星核沿着绝热线的热流的热导系数的作用。在 6-8 GPa 低温时意外的行为可能表明存在未记录的相转变。压力在 10-24 GPa，熔融状态时熔融边界的固态和液态两侧的电阻率似乎保持在 127 μΩ·cm。水星核幔边界的核侧的绝热热流估计在 21.8-29.5 mW m^{-2}，远高于大部分 Fe-S 或 Fe-Si 核模型，而类似 Fe 核模型。比较这些结果和热演化模型，表明水星发电机保持热驱动持续 0.08-0.22 Gyr，这时核变成亚绝热并受激发从主要的热对流到内核形成导致的化学对流的一个变化。

ABSTRACT: The effect of the core thermal conductivity on the heat flow along the adiabat is investigated using direct measurements of electrical resistivity of Fe8.5Si at pressures from 5-24 GPa and temperatures above melting. Unexpected behaviour at low temperatures between 6-8 GPa may indicate an undocumented phase transition. Measurements of electrical resistivity at melting seem to remain constant at 127 μΩ·cm from 10-24 GPa, on both the solid and liquid side of the melting boundary. The adiabatic heat flow at the core side of Mercury's core-mantle boundary is estimated between 21.8-29.5 mW m^{-2}, considerably higher than most models of an Fe-S or Fe-Si core yet similar to models of an Fe core. Comparing these results with thermal evolution models suggests that Mercury's dynamo remained thermally driven up to 0.08-0.22 Gyr, at which point the core became sub-adiabatic and stimulated a change from dominant thermal convection to dominant chemical convection arising from the growth of an

inner core.

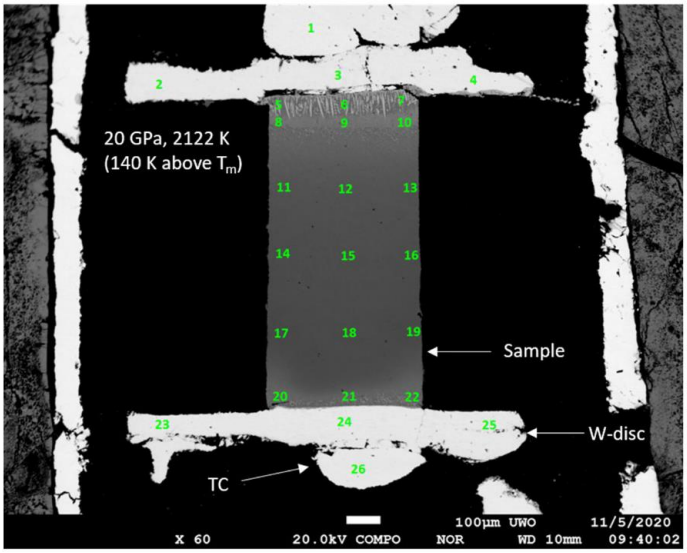

Point #	Si (wt%)	Fe (wt%)	Re (wt%)	W (wt%)	Total (wt%)
1	0.11	0.00	25.95	73.87	99.92
2	0.11	0.00	0.20	98.81	99.12
3	0.11	0.02	0.20	99.37	99.70
4	0.11	0.01	0.21	99.35	99.68
5	5.23	58.20	0.12	36.28	99.83
6	5.31	61.66	0.24	32.61	99.81
7	5.47	67.16	1.01	24.33	97.97
8	6.01	67.19	0.08	25.90	99.19
9	6.01	67.77	0.21	25.31	99.30
10	5.87	66.52	1.01	25.97	99.36
11	7.76	83.84	0.03	7.67	99.30
12	7.73	83.30	0.06	7.92	99.00
13	7.66	83.72	0.12	7.44	98.94
14	8.10	87.10	0.00	4.02	99.22
15	7.97	86.16	0.04	4.69	98.86
16	8.01	86.51	0.05	4.31	98.87
17	8.12	88.19	0.02	2.19	98.51
18	8.14	87.46	0.02	3.24	98.86
19	8.13	88.69	0.05	2.10	98.96
20	6.65	72.84	0.04	19.59	99.13
21	6.69	73.68	0.06	18.14	98.57
22	6.09	69.70	0.08	22.53	98.39
23	0.11	0.01	0.14	99.18	99.44
24	0.11	0.02	0.17	99.04	99.33
25	0.10	0.07	0.20	98.29	98.67
26	0.11	0.02	5.24	94.44	99.81

Figure 1. Cross-sectional view of a Fe-8.5Si sample quenched from 20 GPa and 2122 K, along with the chemical analysis. The sample, W-discs and TC are indicated on the cross-sectional view.

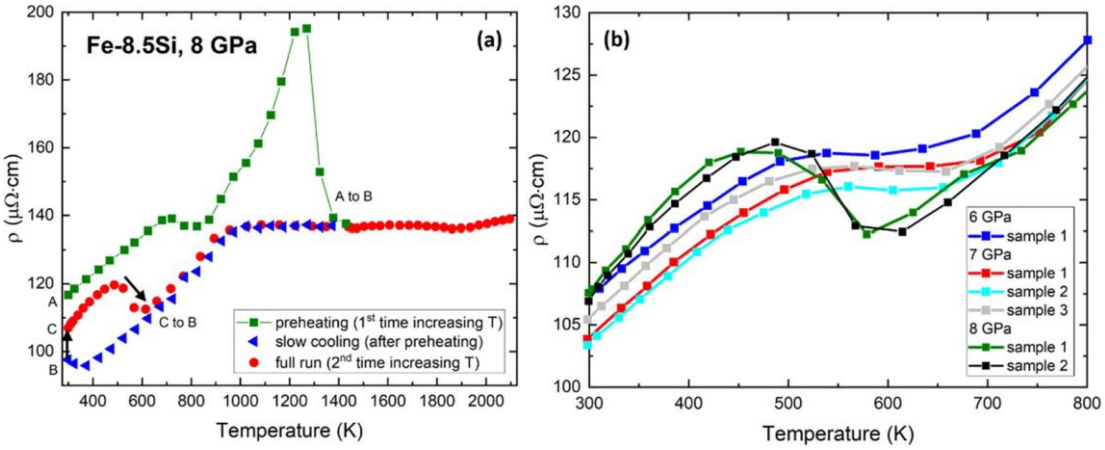

Figure 2. (a) Electrical resistivity measurements of Fe-8.5Si at 8 GPa showing a hysteresis loop. The starting material is labelled as Phase A. (b) Repeated runs at 6-8 GPa showing consistent behaviour at low T. The T is first increased until approximately 1400 K, at which point the electrical resistivity measurement reached the expected value (phase B). The sample is then slowly cooled down to room T. Once at room T, the electrical resistivity value increases until it stabilises (phase C). The T is increased a second time and a transition between phase C and phase B is observed.

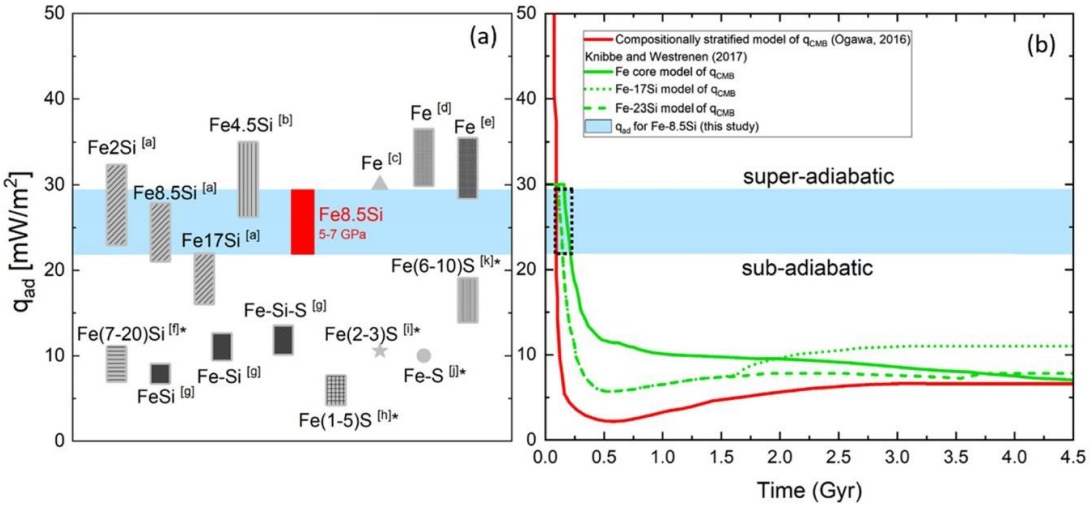

Figure 3. (a) The core adiabatic heat flux at Mercury's CMB for an Fe-8.5Si core calculated in this study and shown by the shaded blue area, compared to the literature values for different compositions. The data are labelled by the compositions and the letters give the reference. Reference [a] Berrada et al. (2020), [b] Silber et al. (2019), [c] Ezenwa and Secco (2019), [d] Silber et al. (2018), [e] Deng et al. (2013), [f] Knibbe and van Westrenen (2018), [g] Pommier (2019), [h] Stevenson et al. (1983), [i] Schubert et al. (1988), [j] Christensen (2006), and [k] Tosi et al. (2013). The * denotes theoretical studies. (b) Three models of heat flux through Mercury's CMB calculated by Ogawa (2016) and Knibbe and van Westrenen (2017). The horizontal edges of the black dotted rectangle show the range of qad determined in this study for a core composition of Fe-8.5Si. The vertical edges of the black dotted rectangle show the corresponding range of ages of 0.08-0.22 Gyr based on the three models plotted, before which the core was super-adiabatic and after which the core is sub-adiabatic.

4. 高度各向异性的伊比利亚考古遗址的倾角浅化对考古古地磁定年的影响

翻译人：柳加波 liujb@sustech.edu.cn

Palencia-Ortas A, Molina-Cardín A, Osete M L, et al. ***Inclination flattening effect in highly anisotropic archaeological structures from Iberia. Influence on archaeomagnetic dating****[J]. Physics of the Earth and Planetary Interiors, 2021: 106762.*

https://doi.org/10.1016/j.pepi.2021.106762

摘要：定向考古古地磁很少研究燃烧遗址是否具有热剩磁各向异性（ATRM）。我们观察到在特定情况下，ATRM 会干扰古地磁的方向，例如小炉床底部较薄的烘烤粘土。本文重新检查了 56 个伊比利亚燃烧遗址的数据，并利用这些数据分析了 ATRM 对古地磁方向的影响。在高度各向异性的遗址中，倾角变浅（可达 13°）可以通过 ATRM 的张量进行充分校正。本研究表明缺乏各向异性校正的方向数据会极大地干扰考古古地磁定年的结果。在未来考古古地磁研究中，系统分析 ATRM 具有重要意义。

ABSTRACT: In directional archaeomagnetic studies, it is rarely analysed whether the combustion structures display anisotropy of their thermoremanent magnetization (ATRM). It has been observed that, in specific cases like thin baked clays from the base of small hearths, archaeomagnetic directions can also be disturbed by the ATRM. We re-examine data from 56 combustion structures from Iberia and use them to analyse the ATRM effect on their archaeomagnetic directions. Flattening of inclinations up to 13o has been found in highly anisotropic structures that can be adequately corrected by the ATRM tensors. We show how the lack of anisotropy corrections on directional values can dramatically deteriorate the ages obtained from archaeomagnetic dating, highlighting the importance of systematically analysing this property in future archaeomagnetic studies.

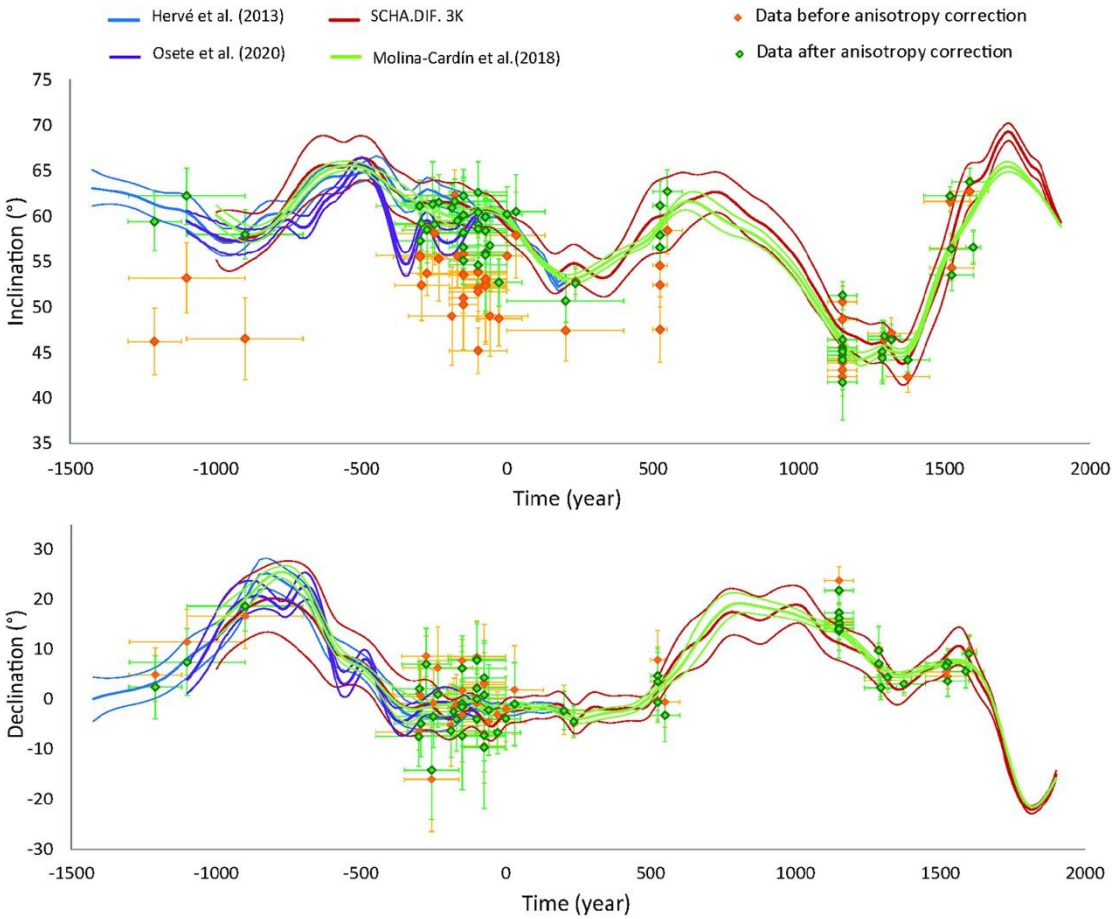

Figure 1. Inclination and declination versus time at Madrid coordinates (data before/after ATRM corrections in yellow/green) together with the SCHA.DIF.3k model for Europe (Pavón-Carrasco et al., 2009) in red, PSVC by Hervé et al. (2013) in blue, PSVC by Molina-Cardín et al. (2018) in green and PSVC by Osete et al. (2020) in purple.

5. 应用超高灵敏度扫描超导显微镜对南太平洋汤加王国洞穴堆积物进行高分辨率磁测

翻译人：张琪 zhangq7@sustech.edu.cn

Fukuyo N, Oda H, Yokoyama Y, et al. ***High spatial resolution magnetic mapping using ultra-high sensitivity scanning SQUID microscopy on a speleothem from the Kingdom of Tonga, southern Pacific****[J]. Earth, Planets and Space, 2021, 73, 77.*

https://doi.org/10.1186/s40623-021-01401-8

摘要：洞穴堆积物是环境磁性和古地磁的理想研究对象，因为它们在稳定的条件下记录了连续的磁信号，可以使用 U 系列和放射性碳法进行可靠的放射性测年。然而，它们微弱的磁信号阻碍了其在地球科学领域的广泛使用。虽然以往的研究已经成功地重建了古地磁和古环境变化信息，但所给出的时间分辨率并不够。最近在这一领域出现的扫描 SQUID 超导显微镜（SSM）可以在保持高空间分辨率的弱磁场成像，可能能够克服以往的障碍。此研究中，作者利用 SSM 对汤加王国汤加 Tongatapu 岛 Anahulu 洞穴采集的石笋样品进行高空间分辨率磁测。5 mT 交变磁场退磁后测得的平均磁场约为 0.27 nT，传感器-样品距离为~200μm。与白色内部（0.09 nT）相比，灰色表层观测到更强的磁场（平均约 0.62 nT），此外洞穴堆积物亚毫米尺度上的层状结构，使得 SSM 的扫描分辨率与洞穴化石的年增长率相相当。通过等温剩磁反演（IRM）计算得出的岩样磁化强度也表明，表层的磁性矿物含量高于内部。此特征被低温磁测法进一步的观测到。结果表明，所研究洞穴堆积物的磁性载体主要为磁铁矿和磁赤铁矿，可能含有赤铁矿或 ε-Fe_2O_3。一阶反转曲线（FORC）的测量和 IRM 获得曲线表明，该洞穴堆积物中含有不同矫顽力和磁畴状态的磁性矿物混合物。磁赤铁矿对灰色表层总磁化强度的贡献远大于白色内部。灰白色表层与内部磁性矿物特征的差异可以表明沉积环境的变化可能是氧化环境引起的。

ABSTRACT: Speleothems are ideal archives of environmental magnetism and paleomagnetism, since they retain continuous magnetic signals in stable conditions and

can be used for reliable radiometric dating using U-series and radiocarbon methods. However, their weak magnetic signals hinder the widespread use of this archive in the field of geoscience. While previous studies successfully reconstructed paleomagnetic signatures and paleoenvironmental changes, the time resolutions presented were insufficient. Recently emerging scanning SQUID microscopy (SSM) in this field can image very weak magnetic fields while maintaining high spatial resolution that could likely overcome this obstacle. In this study, we employed SSM for high spatial resolution magnetic mapping on a stalagmite collected at Anahulu cave in Tongatapu Island, the Kingdom of Tonga. The average measured magnetic field after 5 mT alternating field demagnetization is ca. 0.27 nT with a sensor-to-sample distance of ~ 200 μm. A stronger magnetic field (average: ca. 0.62 nT) was observed above the grayish surface layer compared to that of the white inner part (average: ca. 0.09 nT) associated with the laminated structures of the speleothem at the submillimeter scale, which scanning resolution of the SSM in this study is comparable to the annual growth rates of the speleothem. The magnetization of the speleothem sample calculated from an inversion of isothermal remanent magnetization (IRM) also suggests that the magnetic mineral content in the surface layer is higher than the inner part. This feature was further investigated by low-temperature magnetometry. Our results show that the main magnetic carriers of the speleothem under study are magnetite and maghemite and it can contain hematite or ε-Fe_2O_3. The first-order reversal curve (FORC) measurements and the decomposition of IRM curves show that this speleothem contains a mixture of magnetic minerals with different coercivities and domain states. The contribution from maghemite to the total magnetization of the grayish surface layer was much higher than the white inner part. Such differences in magnetic mineralogy of the grayish surface layer from that of the inner part suggest that the depositional environment shifted and was likely changed due to the oxidative environment.

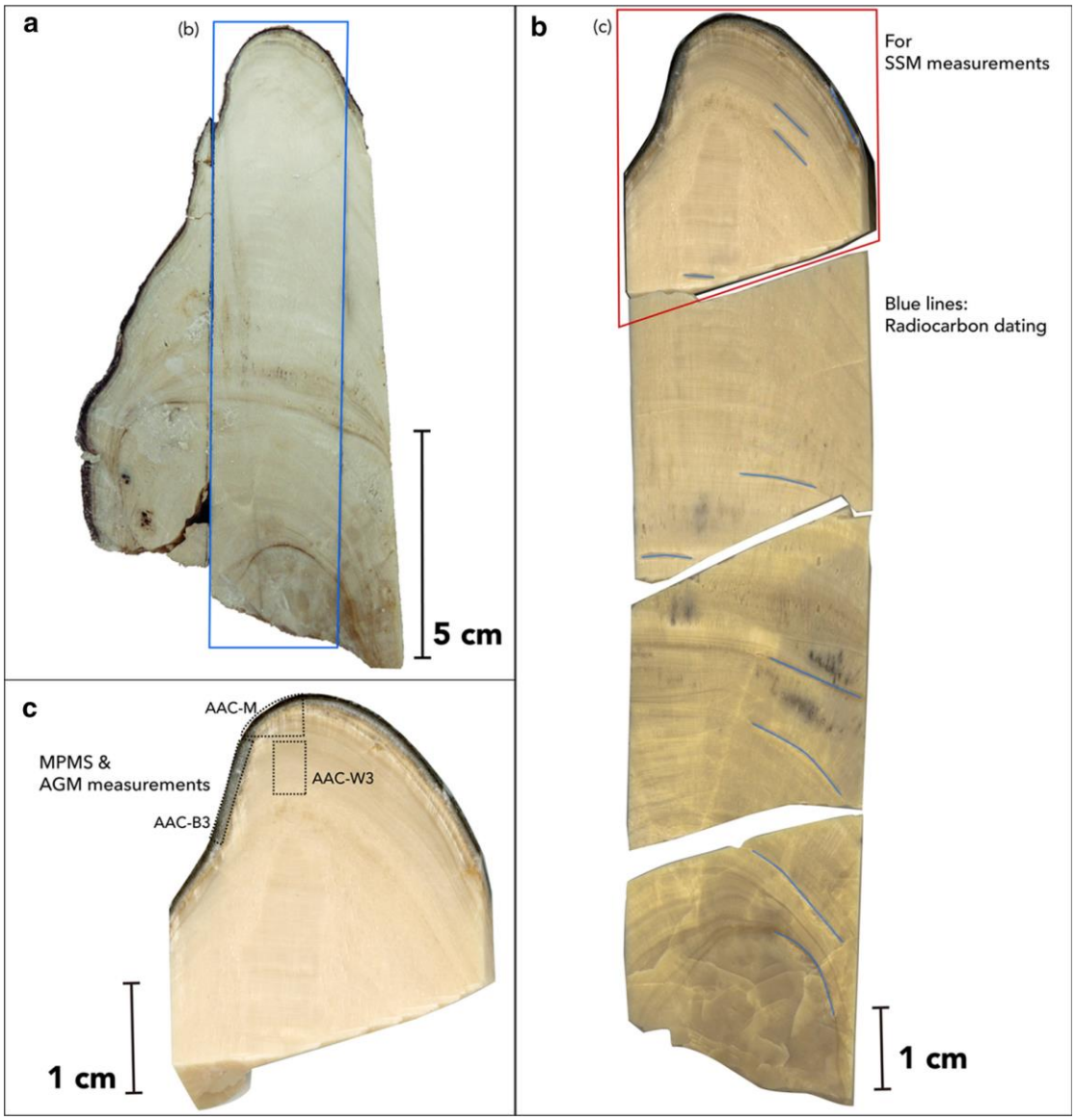

Figure 1. a Photo of a half-split sample of a speleothem; b SSM measurements and ^{14}C dating; and c MPMS and AGM measurements.

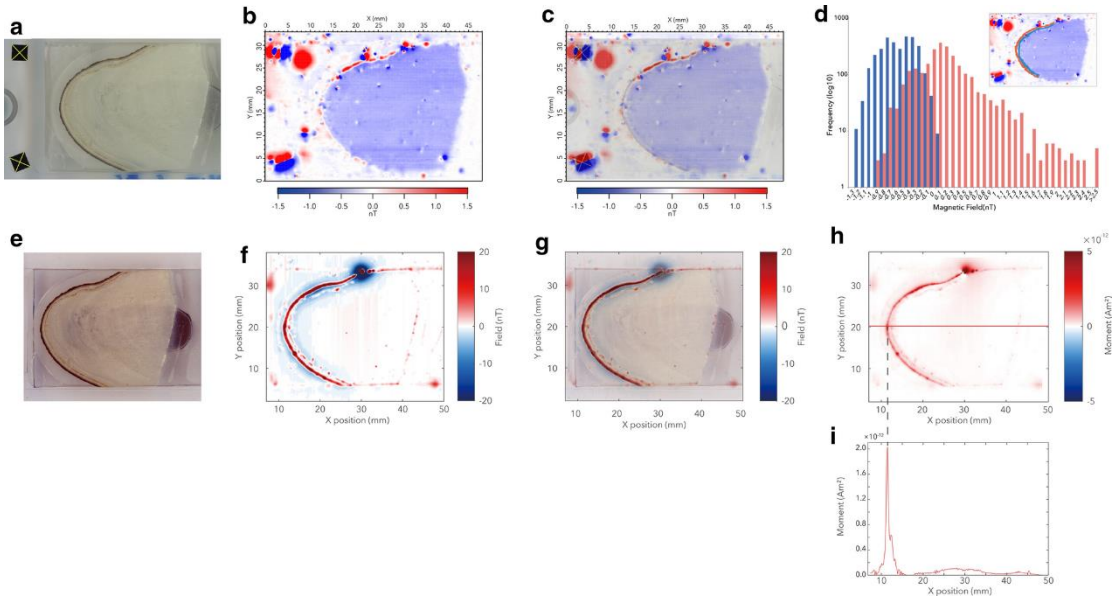

Figure 2. Optical and magnetic images of NRM and IRM and their analyses. a Optical image, b magnetic image of NRM, and c optical image overlaid on the magnetic image of NRM. d Distribution of magnetic field within the highly magnetic layer next to the surface and the layer slightly inside with less magnetic feature. Each dataset was selected according to the region shown in the inset figure on the upper-right; i.e., red and blue correspond to the magnetic and less magnetic areas, respectively. e Optical image (contrast has been changed from a for better visibility of the colored surface layers), f magnetic image of IRM (1.4 T), and g optical image overlaid on a magnetic image of IRM (1.4 T). h Magnetic moment distribution of IRM image calculated on 0.2 mm × 0.2 mm grid points from the magnetic field in f. Magnetic moment distributions were calculated, according to Weiss et al. (2007). i Line profile along a horizontal line in h at 20.1 mm of Y position. The range of gray shade is the same as the range of a light green square in h.

6. 全新世中期南亚和东南亚季风：动力降尺度模拟和绿色撒哈拉的影响

翻译人：盖聪聪 gaicc@sustech.edu.cn

Huo Y, Peltier W R, Chandan D, et al. ***Mid-Holocene monsoons in south and southeast Asia: dynamically downscaled simulations and the influence of the Green Sahara****[J]. Climate of the Past, 2021, (17), 1645-1664.*

https://doi.org/10.5194/cp-17-1645-2021

摘要：代用记录表明，由于到达大气层顶部的太阳辐射总量季节性差异变大，全新世中期（MH，6000 年前）的北半球夏季通常比今天温暖，而冬季则更冷。包括北部的喜马拉雅山脉、青藏高原、南部沿印度西海岸的西高止山脉在内的南亚和东南亚地形复杂，造成了区域气候的复杂性。因此，MH 期间夏季风强度和空间变异性的模拟在技术层面上具有挑战性。为了更准确地捕捉季风系统在这些地区的重要区域特征，作者利用耦合气候模型完成了一系列区域气候模拟和动力降尺度的 MH 全球模拟。区域耦合模拟系统包括 UofT-CCSM4、WRF 区域气候模型和三维的 CROCO。在全球模型中，作者小心地加入了绿色撒哈拉边界条件，以便与标准 MH 模拟进行比较并捕捉印度和东南亚地区的绿色撒哈拉与季风环流之间的相互作用。对比模拟和气候重建的结果，作者发现动力降尺度模拟比全球气候模型产生的异常值更真实，尽管二者都低估了降水变化。绿色撒哈拉对南亚和东南亚的季风性降水影响也很大，特别是在南亚和东南亚北部，预测降水会大幅增加，并且季风持续时间会延长。相较于粗糙的全球模型，数据—模型与降尺度模拟的结果更好，在古数据—模型对比中非常有价值。

ABSTRACT: Proxy records suggest that the Northern Hemisphere during the mid-Holocene (MH), to be assumed herein to correspond to 6000 years ago, was generally warmer than today during summer and colder in the winter due to the enhanced seasonal contrast in the amount of solar radiation reaching the top of the atmosphere. The complex orography of both South and Southeast Asia (SA and SEA), which includes the Himalayas and the Tibetan Plateau (TP) in the north and the Western Ghats

mountains along the west coast of India in the south, renders the regional climate complex and the simulation of the intensity and spatial variability of the MH summer monsoon technically challenging. In order to more accurately capture important regional features of the monsoon system in these regions, we have completed a series of regional climate simulations using a coupled modeling system to dynamically downscale MH global simulations. This regional coupled modeling system consists of the University of Toronto version of the Community Climate System Model version 4 (UofT-CCSM4), the Weather Research and Forecasting (WRF) regional climate model, and the 3D Coastal and Regional Ocean Community model (CROCO). In the global model, we have taken care to incorporate Green Sahara (GS) boundary conditions in order to compare with standard MH simulations and to capture interactions between the GS and the monsoon circulations in India and SEA. Comparison of simulated and reconstructed climates suggest that the dynamically downscaled simulations produce significantly more realistic anomalies in the Asian monsoon than the global climate model, although they both continue to underestimate the inferred changes in precipitation based upon reconstructions using climate proxy information. Monsoon precipitation over SA and SEA is also greatly influenced by the inclusion of a GS, with a large increase particularly being predicted over northern SA and SEA, and a lengthening of the monsoon season. Data-model comparisons with downscaled simulations outperform those with the coarser global model, highlighting the crucial role of downscaling in paleo data-model comparison.

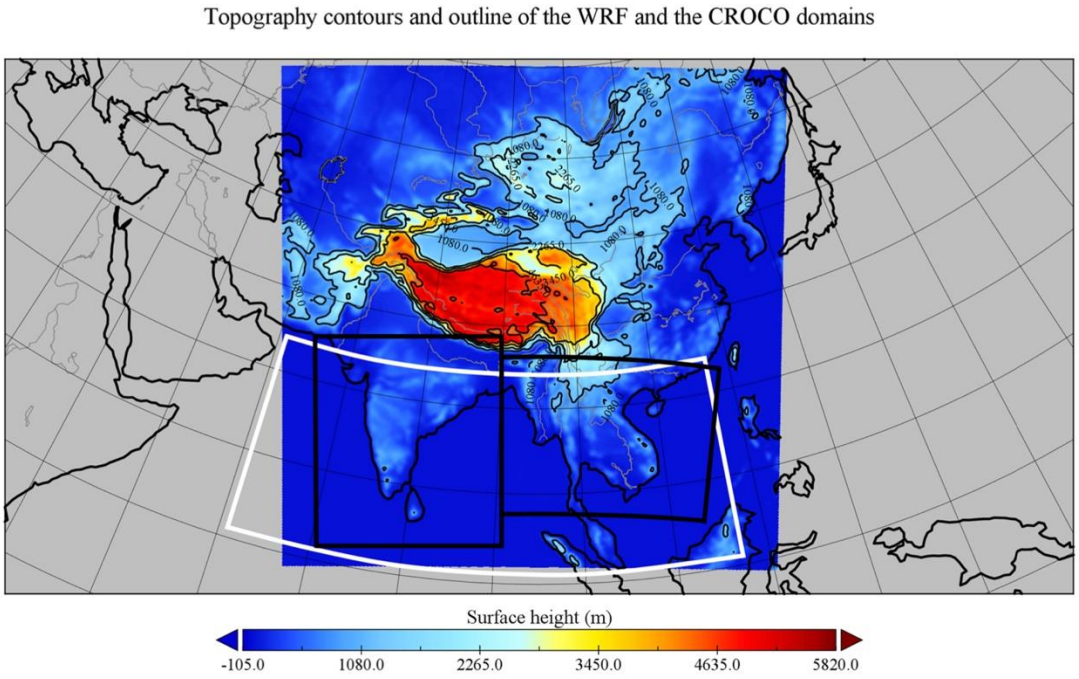

Figure 1. Shaded topography along with the outlines of the (shaded region) WRF and (white rectangle) CROCO domains. The two black rectangles denote the regions used to calculate spatial averages over SA and SEA. Major rivers and lakes are shown in grey contours, and selected topographic heights are shown in thin black contours.

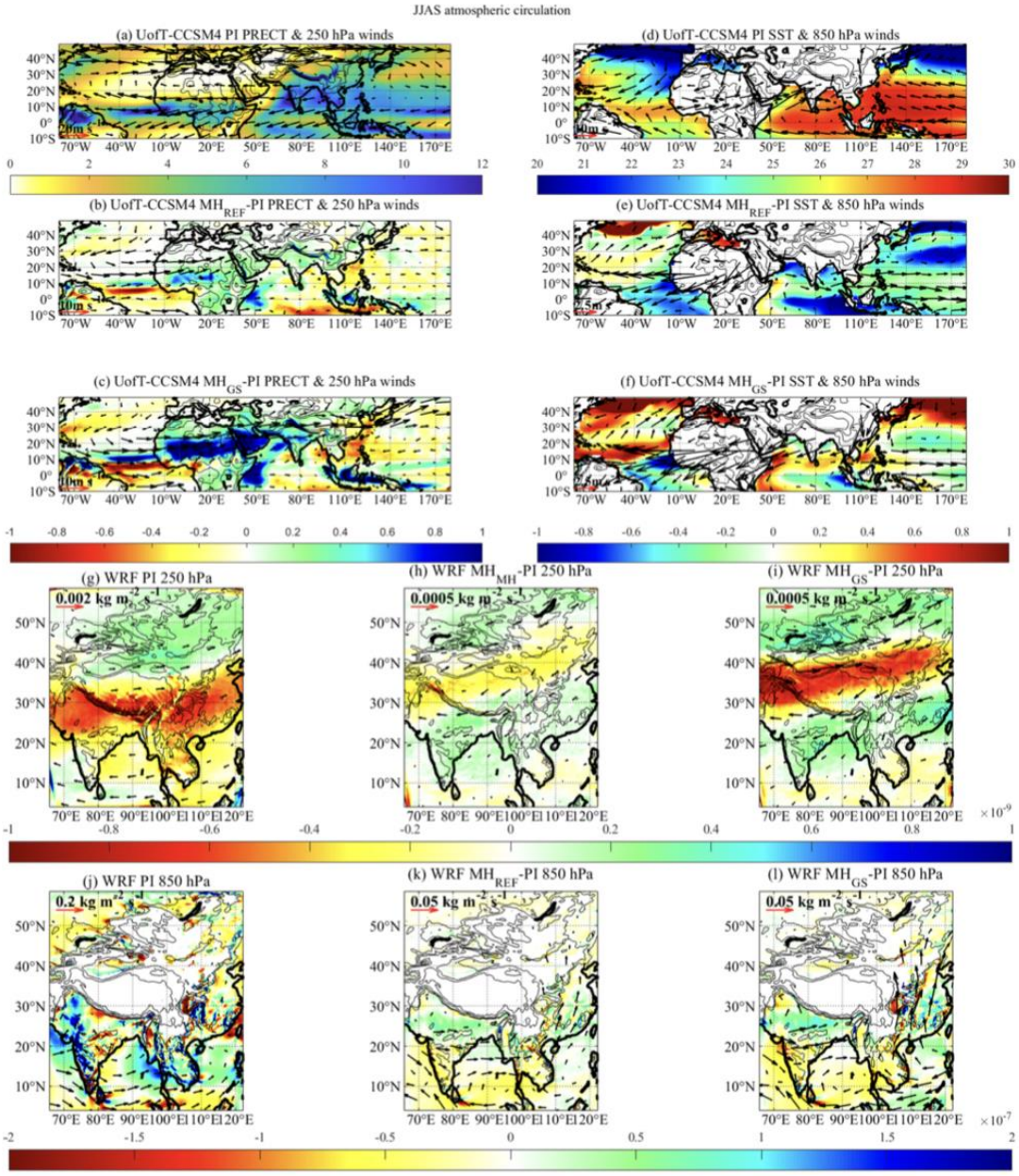

Figure 2. 250 hPa winds (vector, m/s) and precipitation (shaded, mm/d) from the UofT-CCSM4 for (a) the PI simulations and anomalies in (b) MH_{REF} and (c) MH_{GS}. 850 hPa winds (vector, m/s) and SST (shaded, ℃) from the UofT-CCSM4 for (d) the PI simulations and anomalies in (e) MH_{REF} and (f) MH_{GS}. Moisture flux (vector, kg/m^2/s) and its convergence (shaded, kg/m^3/s), with blue indicating convergence (moisture sink) and red divergence (moisture source), for the PI simulations of WRF–CROCO ensemble mean at (g) 250 hPa and (j) 850 hPa. Anomalies of moisture flux (vector, kg/m^2/s) and its convergence (shaded, kg/m^3/s) for (h, k) MHREF and (i, l) MHGS at (h, i) 250 hPa and (k, l) 850 hPa. The topography contours of 500, 1000, 2000, and 4000 m are also shown.

7. 晚中生代古太平洋板块“剪刀式”俯冲：来自中国东南部赣杭构造带的岩浆作用

翻译人：周洋 zhouy3@sustech.edu.cn

Liu B, Zhao X, Yu S, et al. ***Late Mesozoic Paleo-Pacifc Plate “scissors-like” subduction: Insight from the magmatism in the Gan-Hang Belt, Southeast China****[J]. Geological Society of America Bulletin, 2021, 133, 1039–1056.*

https://doi.org/10.1130/B35743.1

摘要：尽管人们普遍认为古太平洋板块向东亚大陆之下俯冲，但关于俯冲的初始时间和地球动力学模型存在很大争议。在这篇文章中，我们报道了中国东南部赣杭构造带花岗岩体的地球化学和年代学特征。大帽山岩体锆石 U-Pb 年龄为 139.60 ± 0.69 Ma 和 133.90 ± 1.70 Ma，千山和凤龙谷岩体的年代分别为 135.70 ± 1.30 Ma 和 135.33 ± 0.93 Ma。河村和黄土岭岩体年龄分别为 157.85 ± 0.77 Ma 和 167.10 ± 7.50 Ma。大帽山岩体主要和微量元素方面具有明显的 A 型花岗岩地球化学特征，例如高 $K_2O + Na_2O$ 含量（平均 8.46 wt%）和 FeO_T/MgO 比值（平均 10.29）。CaO/Na_2O 比值较低及 Al_2O_3/TiO_2（平均为 110.05）、Rb/Ba（平均为 9.14）和 Rb/Sr（平均为 22.53）比值较高。同时，我们还研究了赣杭构造带中与挤压构造环境中形成的岩浆矿有关的中生代埃达克岩以及后期在张性构造环境中形成的双峰岩墙和 A 型花岗岩。具有埃达克地球化学特征的岩体与岛弧特征的岩体（175-150 Ma）与古太平洋板块北西俯冲有关，双峰岩墙和 A 型花岗岩（135-123 Ma）与俯冲板片回撤有关。这些岩体都显示出同位素年龄从内陆到沿海，从西南到东北逐渐变年轻的趋势。我们认为这些岩体在中国东南部的分布格局受古太平洋板块剪刀状俯冲和板片回撤控制，大约在中侏罗世到早白垩世，沿着大陆边缘呈南西至北东方向发生。

ABSTRACT: Though it is widely accepted that the Paleo-Pacifc Plate has a subducted beneath the eastern Asian continent, controversy still exists regarding the initial timing and geodynamic model of the subduction. In this contribution, we report new

geochronology and geochemical data of granitic plutons within the Gan-Hang Belt in Southeast China. The Damaoshan pluton yields zircon U-Pb ages of 139.60 ± 0.69 Ma and 133.90 ± 1.70 Ma, and the Qianshan and Fenglonggu plutons are dated at 135.70 ± 1.30 Ma and 135.33 ± 0.93 Ma, respectively. The Hecun and Huangtuling plutons yield ages of 157.85 ± 0.77 Ma and 167.10 ± 7.50 Ma, respectively. The Damaoshan pluton has an obvious A-type geochemical signature in terms of major and trace element compositions, such as high $K_2O + Na_2O$ contents (average 8.46 wt%) and FeO_T/MgO ratios (average 10.29). The low CaO/Na_2O ratios but high Al_2O_3/TiO_2 (average is 110.05), Rb/Ba (average is 9.14), and Rb/Sr (average is 22.53) ratios indicate a derivation from pelite-derived melt. Meanwhile, we also studied the Mesozoic adakites related to magmatic ore formed during a compressive tectonic setting as well as the later bimodal dikes and A-type granitic plutons formed during the extensional tectonic setting in the Gan-Hang Belt. The multiphase qualitative plutons with geochemical characteristics of the adakitic and island arc types (175-150 Ma) related to the northwestward subduction of the PaleoPacifc Plate, several bimodal dikes, and A-type granitic plutons (135-123 Ma) related to the subducted slab roll-back are found within the Gan-Hang Belt. All of these plutons show a decreasing trend of isotopic ages from the inland area to the coast, from SW to NE. We propose that the distribution pattern of these plutons in Southeast China was controlled by a scissors-like subduction and slab roll-back of the Paleo-Pacifc Plate, which occurred roughly from SW to NE along the continental margin approximately during the Middle Jurassic to the Early Cretaceous.

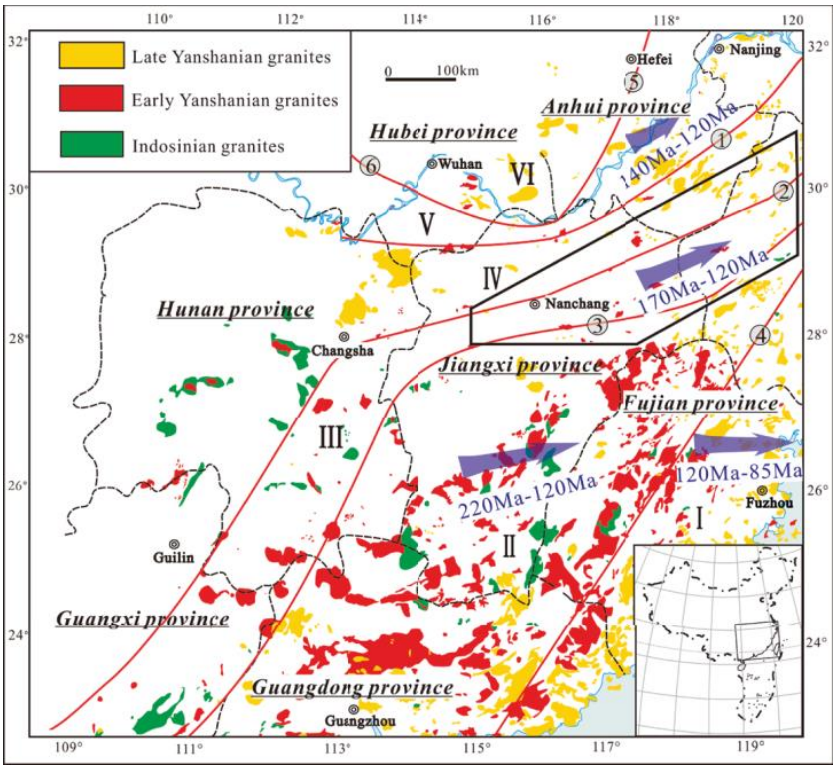

Figure 1. The distribution of the Mesozoic granites in the southeast South China Craton is shown (modifed from Liu et al., 2016). The black arrow represents the subduction direction of Paleo-Pacifc oceanic crust, and the purple arrow represents the migration of magmatism. The locations of the faults are as follows: (1) Nantong-south of Liyang-south of LushanRuichang-Chongyang fault. (2) Hangzhou-Xiangtan-JinxiuPingxiang fault, as the northwestern margin of the Qin-Hang Belt. (3) Shaoxing-JiangshanPingxiang-Wuzhou-Hepu fault, as the southeastern margin of the Qin-Hang Belt. (4) YuyaoLishui-Zhenghe-Dapu fault. (5) Tancheng-Lujiang fault. (6) Southern Dabie Mountains fault. I-Southeast Coastal Belt; II-Cathaysia Belt; III-Qin-Hang Belt (northeastern segment named Gan-Hang Belt); IV-South China Inland Belt; V-middle-lower Yangtze River Belt; VI-Sulu-Dabie Belt. The dashed line indicates the provincial boundary. Long blue arrow indicates younging direction of the granites.

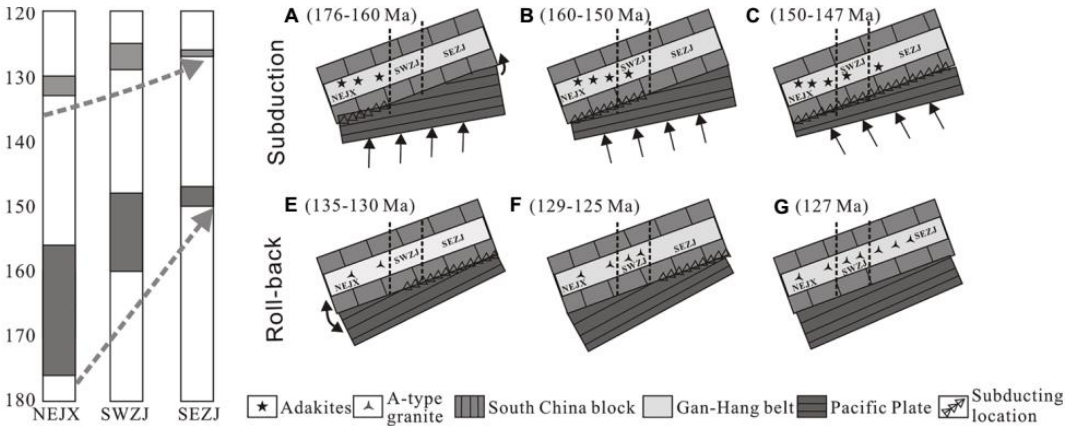

Figure 2. Tectonic model shows the evolution of magmatism in late Mesozoic Southeast China.

8. 白垩纪至中新世西北太平洋板块运动:来自日本 Mineoka 蛇绿混杂岩的古地磁学和 Ar - Ar 年代学约束

翻译人：刘伟 inewway@163.com

Ganbat A, Pastor-Galán D, Hirano N, et al. ***Cretaceous to Miocene NW Pacific Plate Kinematic Constraints: Paleomagnetism and Ar–Ar Geochronology in the Mineoka Ophiolite Mélange (Japan)****[J]. Journal of Geophysical Research: Solid Earth, 2021, 126(5): e2020JB021492. https://doi.org/10.1029/2020JB021492*

摘要：Mineoka 蛇绿混杂岩位于太平洋板块、菲律宾海板块、欧亚板块和北美板块的交汇处。其成因一直有争议，认为它是完全俯冲的板块或太平洋和菲律宾海板块的一部分。本文根据最新的古地磁资料和玄武岩的全岩 $^{40}Ar/^{39}Ar$ 年龄，对 Mineoka 蛇绿混杂岩及其与太平洋板块的关系进行了运动学重建。在对古纬度进行分析的基础上，我们对席状玄武岩进行了构造旋转分析，以推断蛇绿岩的古扩展方向。分析表明，85-80 Ma 形成的枕状洋中脊玄武岩喷发于 16°N，而 50 Ma 形成的玄武岩形成于 34°N。构造旋转分析表明，其扩展方向为 NE 60°。Ar-Ar 年龄显示洋中脊玄武岩年龄为 53-49 Ma，岛弧玄武岩年龄为 41-35 Ma。蛇绿岩的形成发生在西北太平洋 Nemuro-Olyutorsky 弧后扩张时期。我们推断 Izanagi 板块的消亡诱发了俯冲跳跃，并翻转了其极性。在菲律宾海板块向北移动的过程中，一块原始的弧后板片被困在日本海沟附近，其初始俯冲方向平行于洋脊。太平洋和菲律宾海板块之间的相对运动产生了一个高度不稳定的环境，随后形成了一个俯冲带，它留下了一个被俯冲带包围的小型和短暂的板块（Mineoka）。

ABSTRACT: The Mineoka Ophiolite Mélange is located at the intersection of the Pacific, Philippine Sea, Eurasian, and North American plates. The Mineoka ophiolite origin is disputed, and it has been ascribed to a fully subducted plate or part of the Pacific and Philippine Sea plates. In this paper, we present a kinematic reconstruction of the Mineoka Ophiolite Mélange and its relation with the Pacific Plate, based on new paleomagnetic data and bulk-rock $^{40}Ar/^{39}Ar$ ages of basaltic rocks. In addition to

standard analyses for paleolatitudes, we performed a Net tectonic rotation analysis on sheeted dolerite dikes to infer the paleospreading direction that formed the ophiolite. The analysis shows that 85–80 Ma MOR pillow basalts erupted at a paleolatitude of ~16°N, whereas ~50 Ma basalts formed at ~34°N. Net Tectonic Rotation analysis suggests that the spreading direction was NE 60°. Ar-Ar ages yielded 53-49 Ma for MORBs and 41-35 Ma for island-arc basalts. The formation of this ophiolite occurred in the back-arc spreading of the Nemuro-Olyutorsky arcs of the NW Pacific. It infers that the final consumption of Izanagi below Japan instigated a subduction jump and flipped its polarity. Subduction initiated parallel to the ridge, and a piece of the original back-arc crust got trapped near the Japan trench during the northwards motion of the Philippine Sea Plate. The contrasting motion between the Pacific and the Philippine Sea plates generated a highly unstable setting followed by a subduction zone that left a small-sized and short-lived plate ("Mineoka"), surrounded by subduction zones.

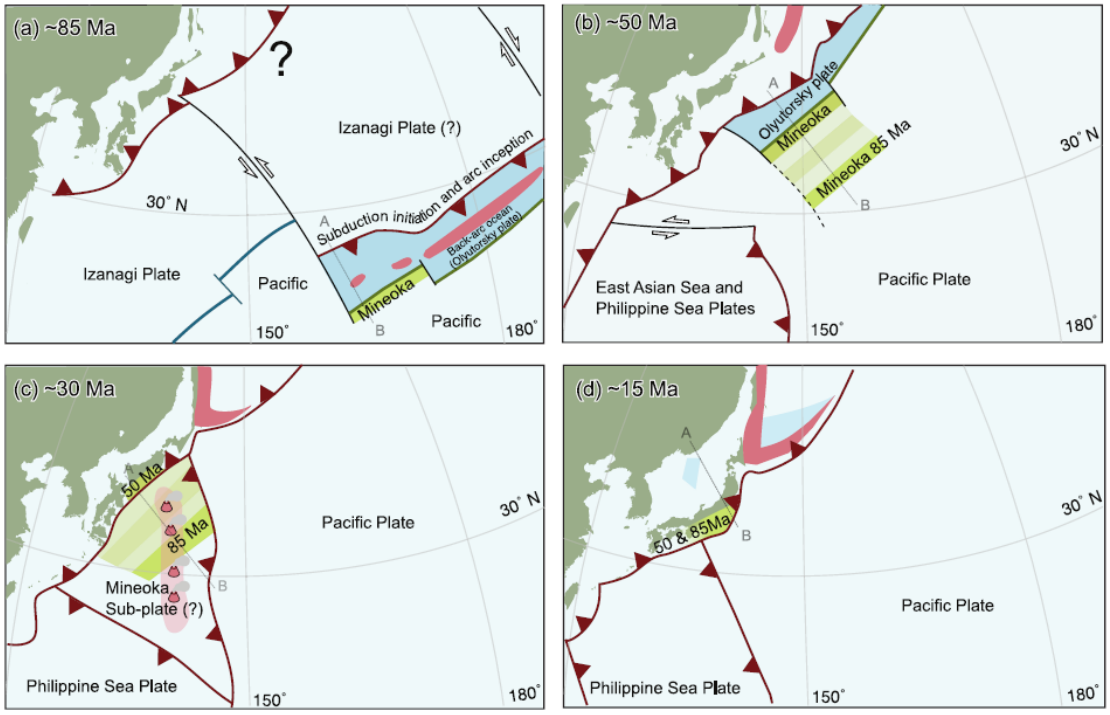

Figure 1. Snapshots of the proposed plate-kinematic reconstruction of the Mineoka ophiolite at NW Pacific region at ca. (a) ~85 Ma, (b) ~50 Ma, (c) ~30 Ma, and (d) ~15 Ma. The red lines represent the reconstructed location of the subduction and triangles are subducting directions. Green lines indicate the

Olyutorsky-Pacific plate boundary and its putative isochron, which has originated as a back-arc after the subduction initiation at ~85 Ma. The blue line marks the mid-ocean ridge between Izanagi and Pacific plates. Pink polygons show Nemuro-Olyutorsky arc, light blue polygons outline newly formed oceanic basins, and solid blue polygon marks Olyutorsky plate. The reconstruction follows the mantle reference frame of Doubrovine et al. (2012).

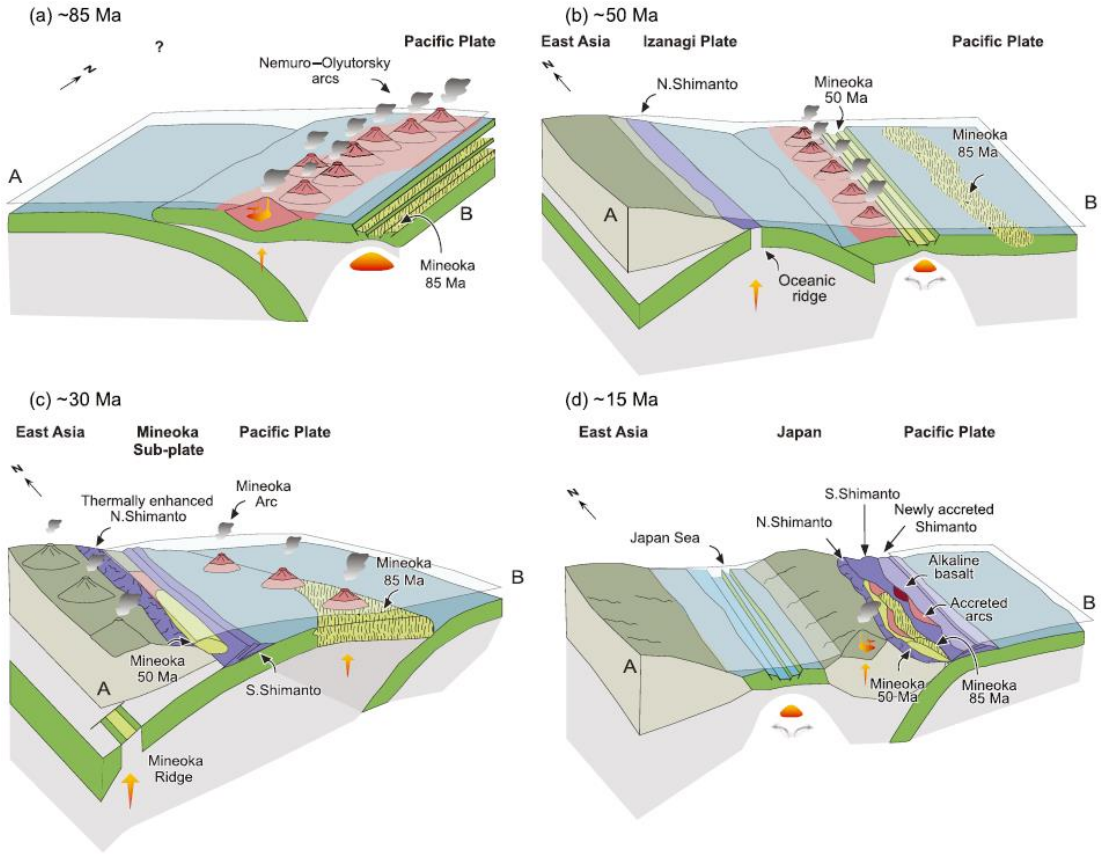

Figure 2. Schematic cross-sections of the proposed plate-kinematic reconstruction of the Mineoka Ophiolite Mélange at NW Pacific region. Locations are shown in Figure 1. (a) ~85 Ma, the birth of the Mineoka ophiolite in the back-arc spreading ridge of Nemuro-Olyutorsky arcs (b) ~50 Ma, continuously forming Mineoka spreading ridge and demise of the Izanagi Plate under the East Asia (c) ~30 Ma, ridge subduction of the Mineoka ridge thermally enhanced the northern Shimanto Belt and the Pacific Plate is subducting under the Mineoka (d) ~15 Ma, Japan Sea opening and fragments from the Mineoka, together with the Shimanto Belt accreted to Japan.

9. 从中国中部石笋 $\delta^{18}O$ 记录看东亚夏季风的全新世变化性

翻译人：杨会会 11849590@mail.sustech.edu.cn

Cai Y J, Cheng X, Ma L, et al. ***Holocene variability of East Asian summer monsoon as viewed from the speleothem $\delta^{18}O$ records in central China****[J]. Earth and Planetary Science Letters, 2021, 558, 116758.*

https://doi.org/10.1016/j.epsl.2021.116758

摘要：中国东部季风降水具有明显的空间分布特征，其变化与东亚夏季风的变化密切相关。中国中部处于南部亚热带湿润气候与北部暖温带半湿润气候的过渡带，是认识和理解东亚夏季风时空变化的核心区域。通过对河南马沟洞 5 根石笋(MG-1、MG-2、MG-7、MG-40 和 MG-64)的 U 系定年和稳定同位素分析，建立了覆盖全新世大部分时间的高分辨率、精确的合成石笋 $\delta^{18}O$ 序列。该合成记录揭示了降水 $\delta^{18}O$ 在 11.7 ~ 1.1 ka BP 之间的变化，平均分辨率约为 4 年。这条马沟合成记录表明，东亚夏季风强度主导了降水 $\delta^{18}O$ 的的长期变化，该变化基本符合北半球夏季日晒（NHSI）的变化趋势。而且，聚合经验模态分解（EEMD）和小波滤波分析揭示长期组分（100-500 年和 500-3000 年）的振幅在 8.5 - 4.9 ka BP 之间略有降低，这意味着在这个温暖时期，气候对百年甚至千年尺度的气候驱动的影响减弱。1-30 年时间尺度的方差相对较低，可能与样品分辨率有关。在与全新世大暖期大致对应的时间段内，确定了包括 8.2 ka 事件在内的 14 个弱东亚夏季风周期。由于在格陵兰冰芯记录中没有发现除 8.2 ka 之外的冷事件，我们初步提出热带海表温度的振荡（SST）可能在其他弱季风事件的引导中起重要作用。将马沟合成记录和其他湿度记录与研究区域的考古记录进行比对，气候变化似乎影响了古代文化的空间分布和农业实践。然而，该地区总体上温和的气候变化，最可能的特征是亚热带湿润气候和暖温带半湿润气候之间的转变，支持了古代文化的普遍连续发展，没有大的中断。

ABSTRACT: Monsoon precipitation in East China shows distinct spatial distribution and its variability is closely linked with the changes of the East Asian summer monsoon

(EASM). Located in the transition zone between the southern subtropical humid climate and the northern warm temperate semi-humid climate, central China is a core region for recognizing and understanding the spatio-temporal variability of the EASM. Using U-series dating and stable isotope analysis on five stalagmites (MG-1, MG-2, MG-7, MG-40 and MG-64) from Magou Cave, Henan Province, Central China, we construct a high-resolution and precisely dated composite stalagmite δ18O time series covering most of the Holocene. This composite record reveals variations in precipitation δ18O between 11.7 and 1.1 ka BP with average resolution of ~4 yrs. The Magou composite record demonstrates that EASM intensity dominates long-term changes in precipitation δ18O, which generally follows the northern hemisphere summer insolation (NHSI) trend. Both, Ensemble Empirical Mode Decomposition (EEMD) and wavelet filtering analyses real that the amplitudes of long term (100-500 and 500-3000 yrs) components were slightly reduced between 8.5 and 4.9 ka BP, implying a weakened influence of climatic forcings on centennial and even millennial timescales during this warm period. Variance on 1-30-yr timescales is relatively low and ascribed to sampling resolution. Fourteen weak EASM intervals, including the 8.2 ka event, were identified within the period corresponding broadly with the Holocene Megathermal. Since no cold excursions other than the 8.2 ka event are found in the Greenland ice core records, we tentatively propose that oscillations in tropical sea surface temperature (SST) likely play an important role in steering other weak monsoon events. Aligning the Magou composite record and other moisture records with archaeological records from the study region, it seems that climate change influenced both the spatial distribution and agricultural practices of ancient cultures. However, overall moderate climatic changes in this region, most likely characterized by shifts between subtropical humid climate and warm temperate semi-humid climate, supported a generally consecutive development of ancient cultures without major hiatuses.

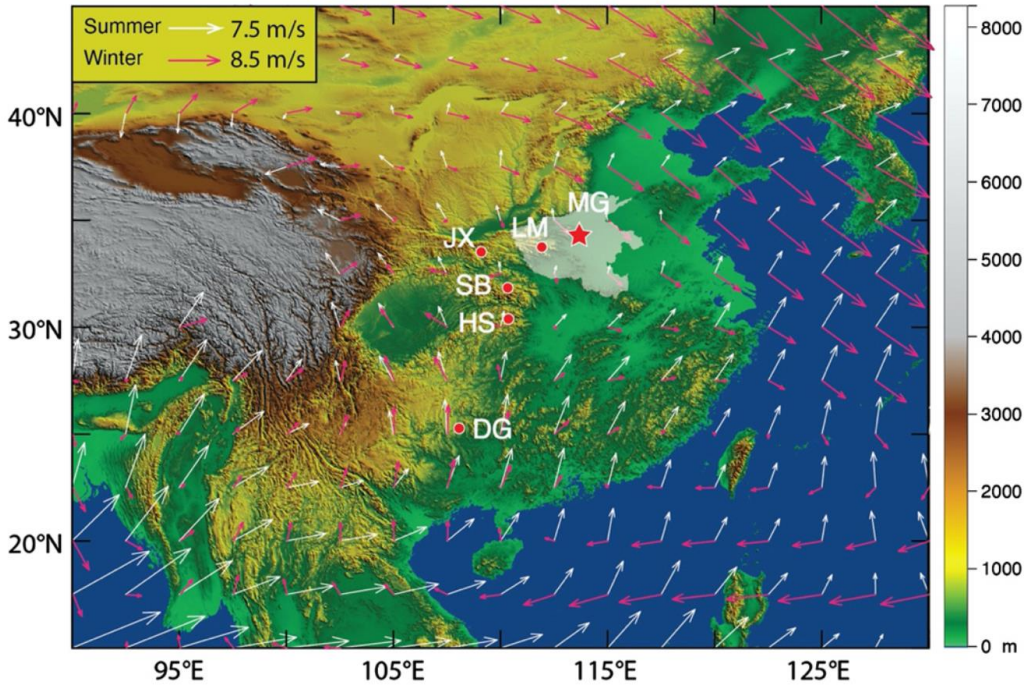

Figure 1. Overview map with the location of the studied cave and relevant records. The topographic map is based on GTOPO 30 data (U.S. Geological Survey's EROS (Earth Resources Observation and Science; http://eros.usgs.gov/#/Find_Data/Products_and_ Data_Available/gtopo30_info) Data Center). White and purple arrows indicate mean summer and winter wind fields at 850 hPa from 1981 to 2010 (NCEP Reanalysis Derived data provided by NOAA/OAR/ESRL PSD, Boulder, Colorado, USA, http://www. esrl.noaa.gov/psd/, Kistler et al., 2001). The location of Magou Cave (MG) is denoted by the red star (113◦23'E, 34◦19'N, ~422 m a.s.l.), all other records are denoted by red circles: LM: Laomu Cave/Dongshiya Cave, 111◦31'E, 33◦48'N, ~840 m a.s.l.; JX: Jiuxian Cave, 109◦6'E, 33◦34'N, ~1495 m a.s.l.; SB: Sanbao Cave, 110◦26'E, 31◦40'N, ~1900 m a.s.l.; HS: Heshang Cave, 110◦25'E, 30◦27'N, ~294 m a.s.l.; DG: Dongge Cave, 108◦5'E, 25◦17'N, ~680 m a.s.l. The white shaded area indicates the Henan Province, largely representing the Central Plain of China.

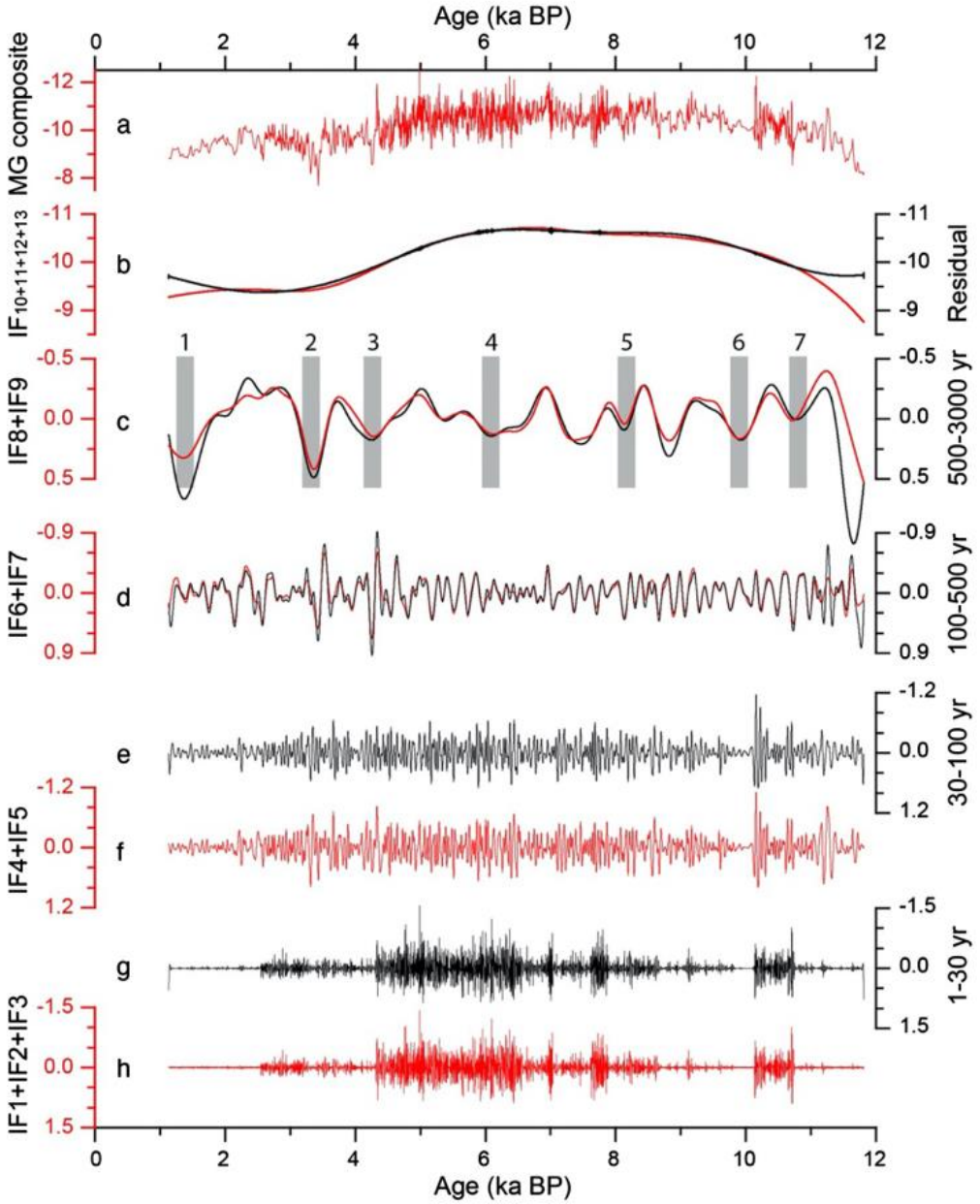

Figure 2. The MG composite time series (a) from ~11.7-1.1 ka BP and derived EEMD components (red) and wavelet band-pass components (black) (b-h). For the EEMD decomposition, noise of 0.2 standard deviations of the data is added for the ensemble calculation, with an ensemble number is 500. Five EEMD components (i.e. sum of components 1-3, sum of components 4-5, sum of components 6-7, sum of components 8-9, and sum of components 10-13) are presented. The wavelet band-pass components indicate the variation of speleothem $\delta^{18}O$ on different timescales and correspond well with the EEMD components.

10. 利用无人机磁测获得小笠原岛弧西岛火山的磁化结构

翻译人：曹伟 11930854@qq.com

Noriko T, Hiroshi I, Masaru N, et al. ***Magnetization structure of Nishinoshima volcano, Ogasawara island arc, obtained from magnetic surveys using an unmanned aerial vehicle****[J]. Journal of Volcanology and Geothermal Research, 2021, online.*

https://doi.org/10.1016/j.jvolgeores.2021.107349

摘要：西岛是小笠原（博宁）岛弧中的一个火山岛，在平静了近 40 年后，自 2013 年 11 月以来，西岛间歇性喷发。通过使用无人机（UAV）系统获取航磁数据，并对数据进行 3D 正则化反演，首次研究了这座不断增长的火山岛的三维（3D）磁化结构。2018 年 9 月和 2019 年 6 月的航磁调查覆盖了约 3 km×3 km 的区域，包括西岛火山的出露部分。我们从观测数据中提取了磁化结构引起的磁异常，并应用结合 L1 和 L2 范数正则化的 3D 反演从异常中模拟磁化结构。我们进行了交叉验证，以同时确定正则化参数和超参数的最佳值。我们发现西岛火山的平均磁化强度约为 3.0 A/m，截至 2019 年，山顶火山口下方和东北侧地表以下几百米深处还存在两个强磁化体。这些特征可能代表了古老冷却岩浆的巨大岩体。这项研究证明了这种相对安全和廉价的观测方法以及这种数据分析方法在调查偏远火山岛磁性结构方面的实用性。今后重复进行这类调查可能使我们能够监测影响火山磁化结构的火山活动。

ABSTRACT: Nishinoshima, a volcanic island in the Ogasawara (Bonin) island arc, has intermittently erupted since November 2013 after a quiescence of nearly 40 years. The three-dimensional (3D) magnetization structure of this growing volcanic island was investigated for the first time by acquiring aeromagnetic data with an unmanned aerial vehicle (UAV) system and subjecting the data to a 3D regularized inversion. The aeromagnetic surveys, in September 2018 and June 2019, covered an area of about 3 km×3 km that included the emergent part of Nishinoshima volcano. We extracted the magnetic anomaly induced by the magnetization structure from the observations and

estimated the magnetization structure from the anomaly by applying the 3D inversion, which combines L1 and L2 norm regularizations. We conducted a cross-validation to simultaneously determine optimum values of a regularization parameter and a hyperparameter. We found that Nishinoshima volcano had an average magnetization of about 3.0 A/m and that two more strongly magnetized bodies existed as of 2019 beneath the summit crater and the northeastern flank at depths several hundred meters below the surface. These features may represent massive bodies of old chilled magma. This study demonstrated the utility of this relatively safe and inexpensive observation method and this data analysis method for investigating the magnetic structure of remote volcanic islands. Repeated future surveys of this type may enable us to monitor volcanic activities that affect the magnetization structure of volcanoes.

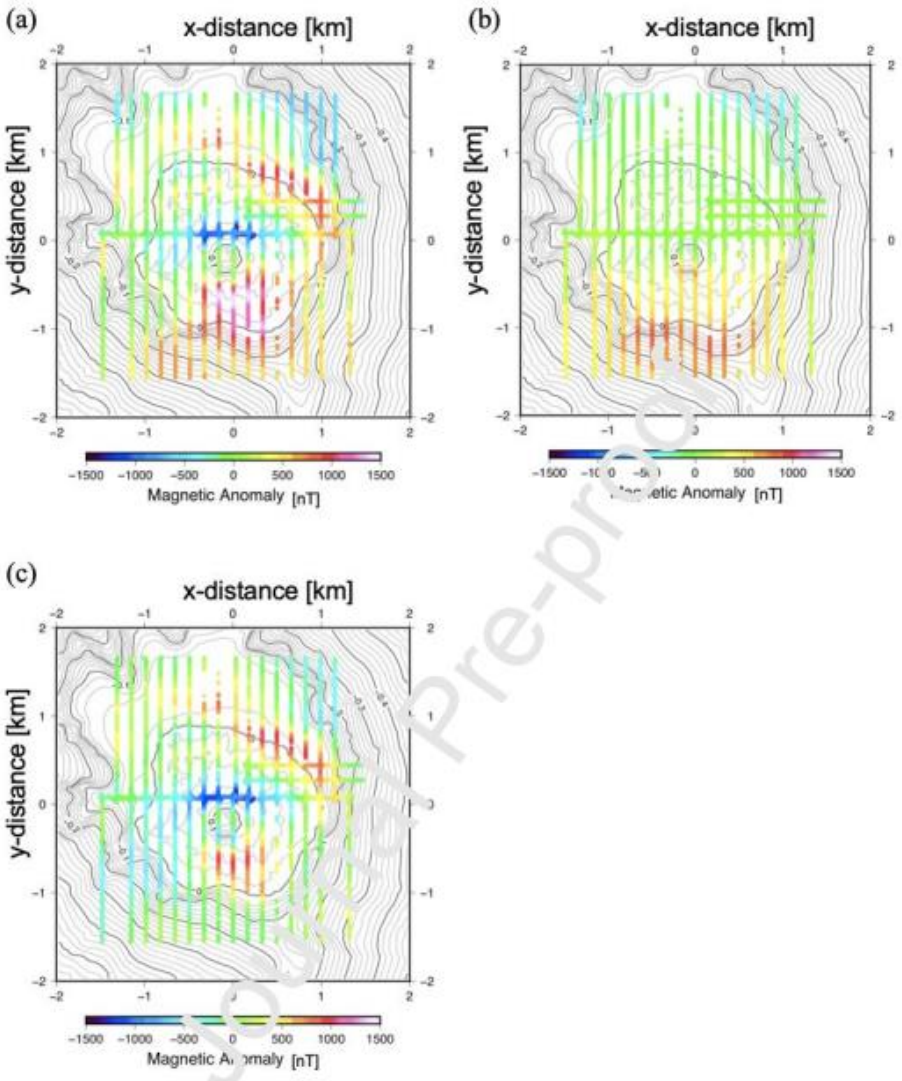

Figure 1. Magnetic anomalies obtained by (a) subtracting the main magnetic field from the observed magnetic intensity, (b) assuming a constant magnetization of 3.0 A/m in Nishinoshima volcano, and (c) subtracting (b) from (a). Black lines are topographic and bathymetric contours; contour interval 20 m.

11. 40 kyrs 以来南海北部湿度的快速变化

翻译人：李海 12031330@mail.sustech.edu.cn

Kaboth-Bahr S, Bahr A, Yamoah K A, et al. ***Rapid humidity changes across the Northern South China Sea during the last ~40 kyrs****[J]. Marine Geology, 2021. 106579.*

https://doi.org/10.1016/j.margeo.2021.106579

摘要：东亚气候的关键是其夏季风系统，它影响着世界上近三分之一的人口。研究结果表明，东亚夏季风（EASM）对气候变暖的主要响应可能是地理范围的变化，而不是强度变化，这将导致东南亚地区在空间上出现洪水和干旱共存的现象。预测 EASM 未来的变化使得研究其过去的变化以及相关的干-湿时空模式变得至关重要。为了了解 EASM 过去的变化，作者对位于南海北部的 ORI-891-16-P1 孔沉积物进行了多种地球化学指标的分析。该孔位于海山顶部，使其对南海北部陆源输入的变化特别敏感，不受海平面引起的影响。利用整个沉积序列的 In(Ti/Ca) 比值，解析 40 kyrs 以来陆源输入的变化。对比前人的研究结果，作者认为末次冰盛期（LGM）具有明显的南北向湿度梯度。这种空间格局与 10-15°夏季风槽从当前位置向南海中心南移一致。叠加在轨道时间尺度波动上，还发现与 H 事件相关的千年尺度变化的强烈迹象。H 事件对东亚夏季风的影响似乎在日照最小值期间被放大，而夏季高日照似乎缓冲了季风系统对这种扰动的影响。作者认为（i）LGM 期间的干-湿分布模拟了未来东亚夏季风变化，（ii）EASM 对大西洋径向反转流减弱的敏感性是自末次冰期以来最强的。

ABSTRACT: A key aspect of East Asian climate is its summer monsoonal system which influences nearly one-third of the world's population. Recent results indicate that the primary response of the East Asian summer monsoon (EASM) to anthropogenic forced climate warming may be a shift in geographical range instead of an intensity change, which would lead to spatial coexistence of floods and droughts over southeastern Asia. The predicted EASM variability in the future has made it paramount to study its past changes and the associated tempo-spatial pattern of aridity and

humidity in its purview. In order to decipher past changes in EASM, we applied a multi-proxy geochemical approach to the sediment core ORI-891-16-P1 located in the northern South China Sea. The position of this sediment core on top of a seamount makes it uniquely sensitive to changes in the terrigenous input into northern South China Sea unbiased by sea level-induced downslope transport processes. Utilizing the ln(Ti/Ca) ratio throughout the sediment sequence we trace terrigenous influx changes reflecting EASM prevalence during the last ~40 kyrs. Based on the comparison of our results to previous studies we infer that the Last Glacial Maximum (LGM; ~20 ka BP) was characterized by a steep N-S humidity gradient. This spatial pattern was in line with a southward shift or contraction of the summer monsoonal trough of 10-15° from its current position toward the centre of the South China Sea. Superimposed on orbital time scale fluctuations we also find strong indication of millennial-scale variability related to Heinrich Stadials. The impact of Heinrich Stadials on the EASM seems amplified during insolation minima, while high summer insolation seems to buffer the monsoonal system to such perturbations. We infer that (i) the humidity-aridity distribution during the LGM mimics predictions of the proposed future EASM configuration, and (ii) that the sensitivity of the EASM to weakening in the Atlantic Meridional Overturning Circulation is the strongest since the last glacial.

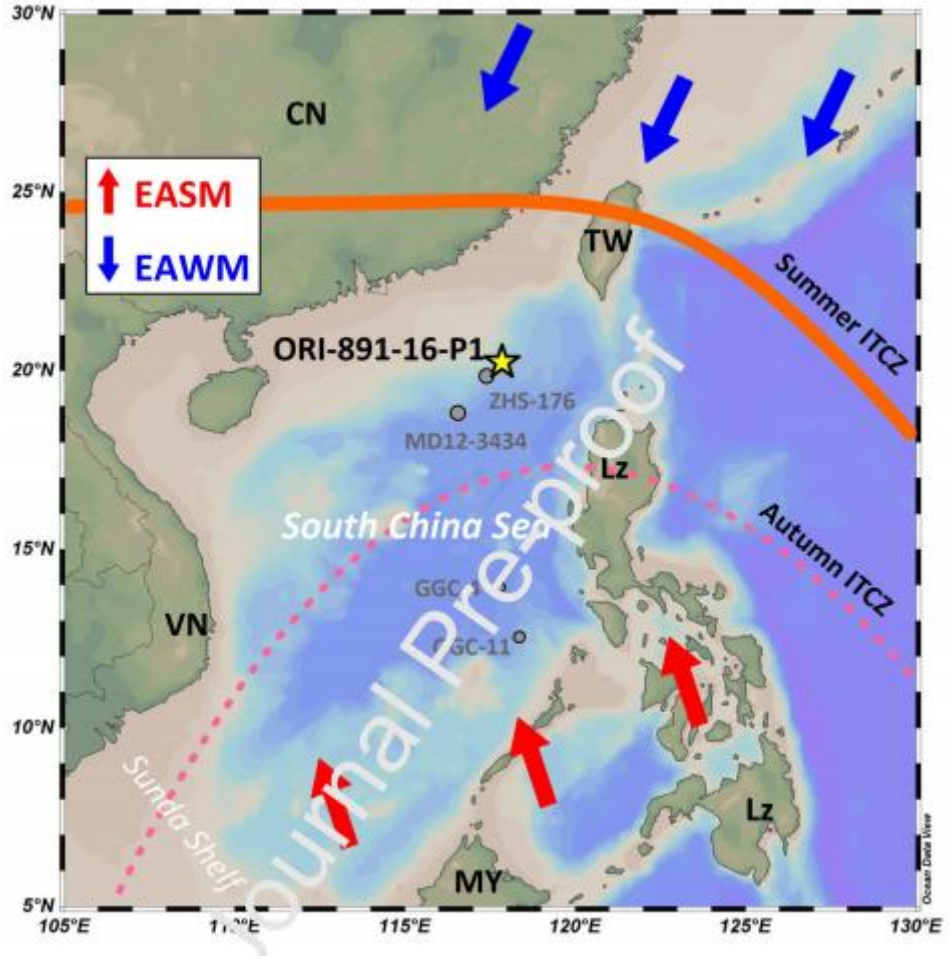

Figure 1. Bathymetric map of the South China Sea (SCS) with the investigated Site ORI-891-16-P1 marked by yellow star. Other sites mentioned in the discussion are marked by grey dots. EAWM = East Asian Winter Monsoon; EASM = East Asian Summer Monsoon; Adjacent countries of the SCS: TW = Taiwan; CN = China; Lz = Luzon; MY = Malaysia; VN = Vietnam. Summer and autumn ITCZ position marked solid orange and dotted orange line, respectively.

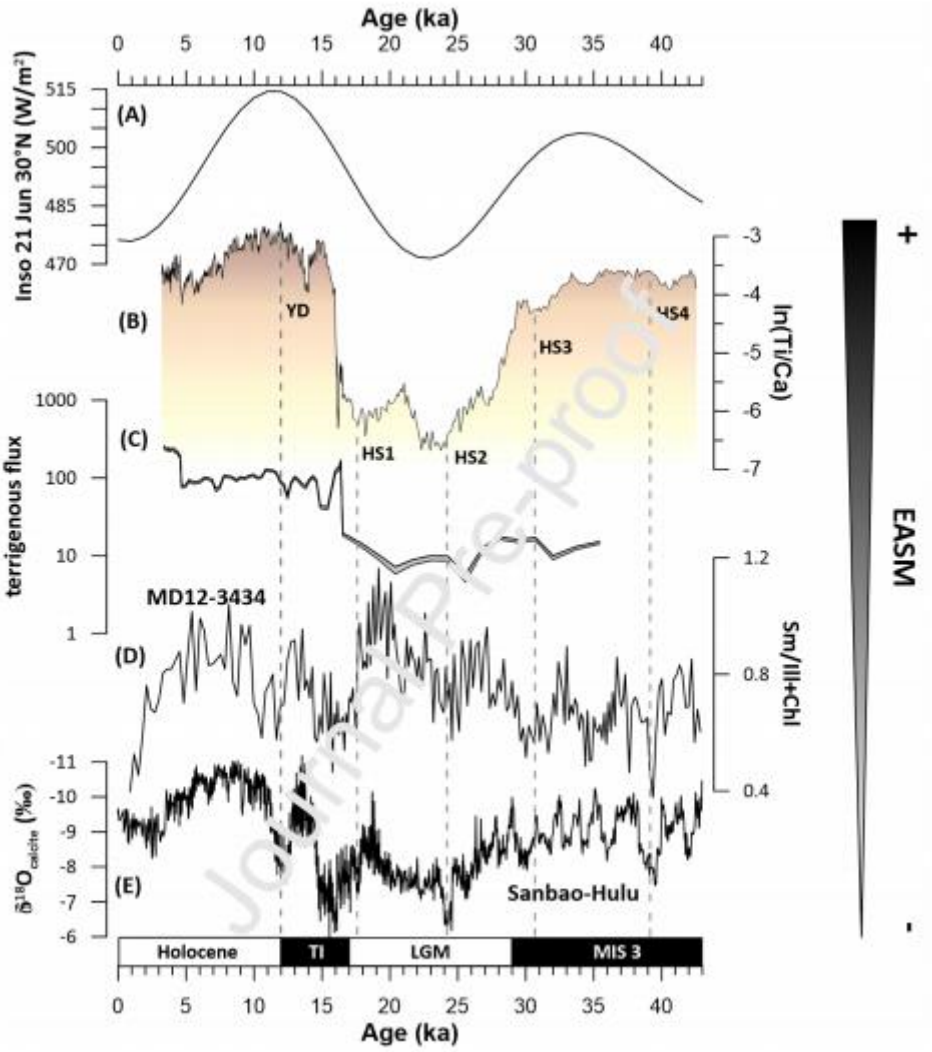

Figure 2. Discussion. (A) Summer (21st June) insolation at 30°N (Laskar et al., 2004); (B) ln(Ti/Ca) ratio from Site ORI-891-16-P1 (this study); (C) terrigenous input from Site ORI-891-16-P1 calculated with 1.6 % opal content (lower line) and 9.4% opal content (upper line) (see section 2.6 for more details on terrigenous influx rate calculation; this study); (D) Smectite/Illite+Chlorite ratio from Site MD12-3434 (Zhao et al., 2018); (E) composite $\delta^{18}O$ speleothem record from Chinese caves Sanbao and Hulu (Wang et al., 2008). Temporal assignment of Holocene, TI, LGM and MIS 3 follows Lisiecki and Raymo, (2005). TI = Termination 1; LGM = Last Glacial Maximum. Allocation of Heinrich Stadials (HS) follows Andrews and Voelker, (2018).

12. Shaw 类绝对古强度方法的改进

翻译人：张伟杰 12031188@mail.sustech.edu.cn

Lloyd S J, Paterson G A, Thallner D, et al. ***Improvements to the Shaw-type absolute palaeointensity method****[J]. Frontiers in Earth Science, 2021, 650.*

https://doi.org/10.3389/feart.2021.701863

摘要：古强度信息使我们能够确定地球磁场在地质时期的强度，为深入了解地球内部提供了一个窗口。获得可靠的测量数据是相当困难的，特别是从较老的岩石中。实验失败的两个最重要的原因是实验室过程中携带剩磁的载磁矿物的改变以及与多畴载磁矿物有关的影响。Shaw 方法是一种被认为可以克服以上两个问题的方法。本文，我们详细介绍并评估了该方法，通过控制实验比较了多种选择标准在主要为前寒武纪岩石的大量非理想数据集的适用性。蒙特卡罗分析被用来确定一组最优的选择标准。最终的结果是得到了一个新的、改进的实验协议，非常适合自动快速 2G 磁强计系统，使实验能够快速和更准确地进行。

ABSTRACT: Palaeointensity information enables us to define the strength of Earth's magnetic field over geological time, providing a window into Earth's deep interior. The difficulties in acquiring reliable measurements are substantial, particularly from older rocks. Two of the most significant causes of experimental failure are laboratory induced alteration of the magnetic remanence carriers and effects relating to multidomain magnetic carriers. One method that has been claimed to overcome both of these problems is the Shaw method. Here we detail and evaluate the method, comparing various selection criteria in a controlled experiment performed on a large, non-ideal dataset of mainly Precambrian rocks. Monte Carlo analyses are used to determine an optimal set of selection criteria; the end result is a new, improved experimental protocol that lends itself very well to the automated Rapid 2G magnetometer system enabling experiments to be carried out expeditiously and with greater accuracy.

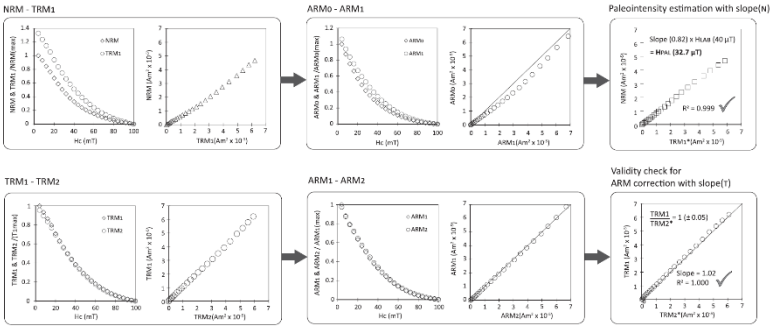

Figure 1. Schematic view of the data analyses process for the Shaw-type experiment using a specimen from Mount Etna. Top row is the palaeointensity experiment, where any alteration to the TRM1 demagnetisation spectra is corrected by multiplying by the ARM slope (ARM0/ARM1) to produce TRM1*. Bottom row is a repeat experiment to test the validity of the ARM corrections. This ARM validity check uses additional remanence acquisitions (TRM2 and ARM2) and should produce a unit slope. Note that the values shown in these figures are after vectoral subtraction of the remanences at the maximum AF step.

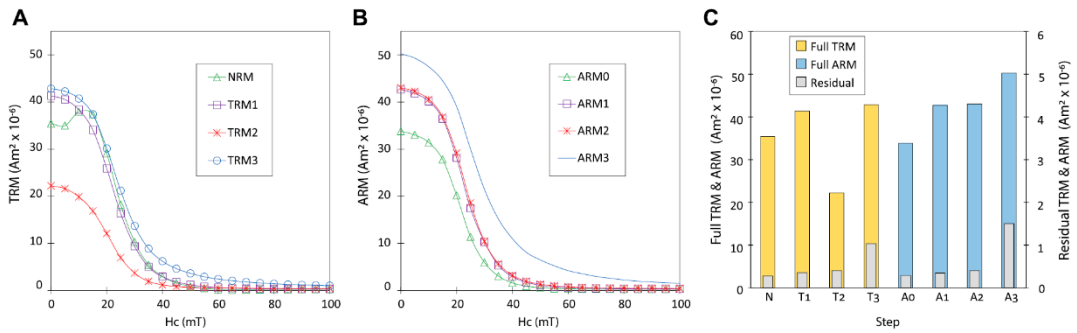

Figure 2. AF demagnetisation spectra of three specimens (6.1A, 2A and 3C) from site MD6. These are vector subtracted as used in the calculation of the slopes (for information on residual magnetisations, see Supplementary Figure S5).

13. 冰期—间冰期尺度上稳定的大西洋深水来源

翻译人：张亚南 zhangyn3@mail.sustech.edu.cn

Pöppelmeier F, Gutjahr M, Blaser P, et al. ***Stable Atlantic Deep Water Mass Sourcing on Glacial-Interglacial Timescales****[J]. Geophysical Research Letters, 2021,48, e2021GL092722. https://doi.org/10.1029/2021GL092722*

摘要：在过去的冰期期间，增加的深海碳储库经常被认为是降低大气中 CO_2 浓度的主要碳汇。为了更好的理解海洋变化对海洋碳储库增加的促进作用，作者通过重建北大西洋 U1313 站位近 100 kyr 的自生 Nd 同位素来评估大西洋深水来源的变化。考虑到对北部 Nd 同位素端元的新限制，作者发现经向和盆地内水团梯度仅有微弱的长期变化，表明了在过去 100 kyr 时间里北源水（NSW）的普遍性存在。初步结果表明，MIS 4 期间 NSW 在赤道和东北大西洋增加了 15%，这对冰期寒冷气候促进南源水扩张的概念提出了质疑。

ABSTRACT: Increased deep ocean carbon storage is often invoked as the major sink for lower atmospheric CO_2 concentrations during past ice ages. In order to improve the understanding of the changes in ocean dynamics facilitating such increased oceanic carbon storage, we assess the variability of deep water provenance in the Atlantic by reconstructing authigenic Nd isotopes from North Atlantic site U1313 over the past ~100 kyr. Under consideration of these new constraints for the northern Nd isotope end-member, we find only limited long-term variations in the meridional and intra-basin water-mass gradients suggesting a prevalence of northern-sourced water (NSW) throughout the past 100 kyr. Tentative results suggest that during the glacial period of Marine Isotope Stage 4 NSW proportions even increased by additional ~15% in the equatorial and Northeast Atlantic, calling into question the notion that cold climates promote the expansion of southern-sourced water.

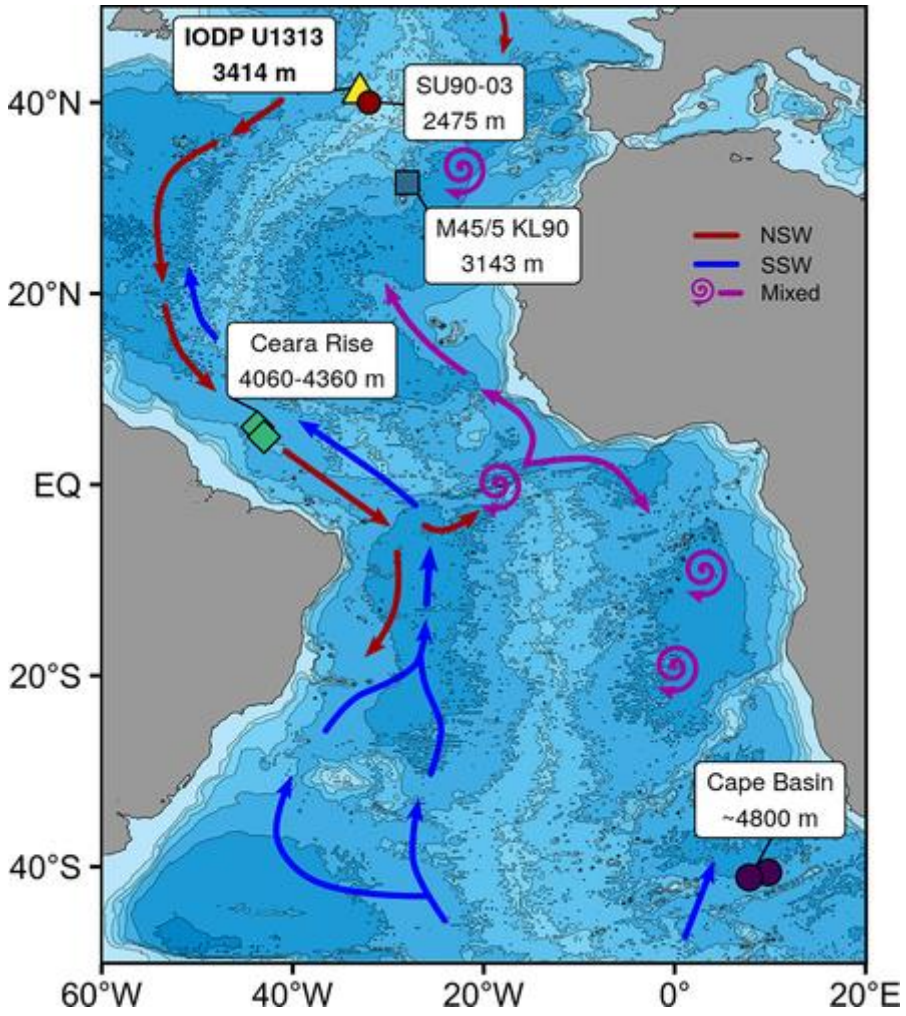

Figure 1. Modern hydrography and site locations. New εNd data from site U1313 are compared to records from M45/5 KL90 (Pöppelmeier, Frank, et al., 2020), SU90-03 (Howe, Piotrowski, Noble, et al., 2016), the Ceara Rise (ODP 929, Howe & Piotrowski, 2017; EW9209-1, Curry & Oppo, 1997) and the composite of two sites from the Cape Basin (RC11-83 and TN057-21 (Piotrowski et al., 2004, 2005)). Blue and red arrows indicate southern sourced water (SSW) and northern sourced water (NSW), respectively. Purple arrows mark mixtures of NSW and SSW, with spirals indicating areas of strongly mixed deep water.

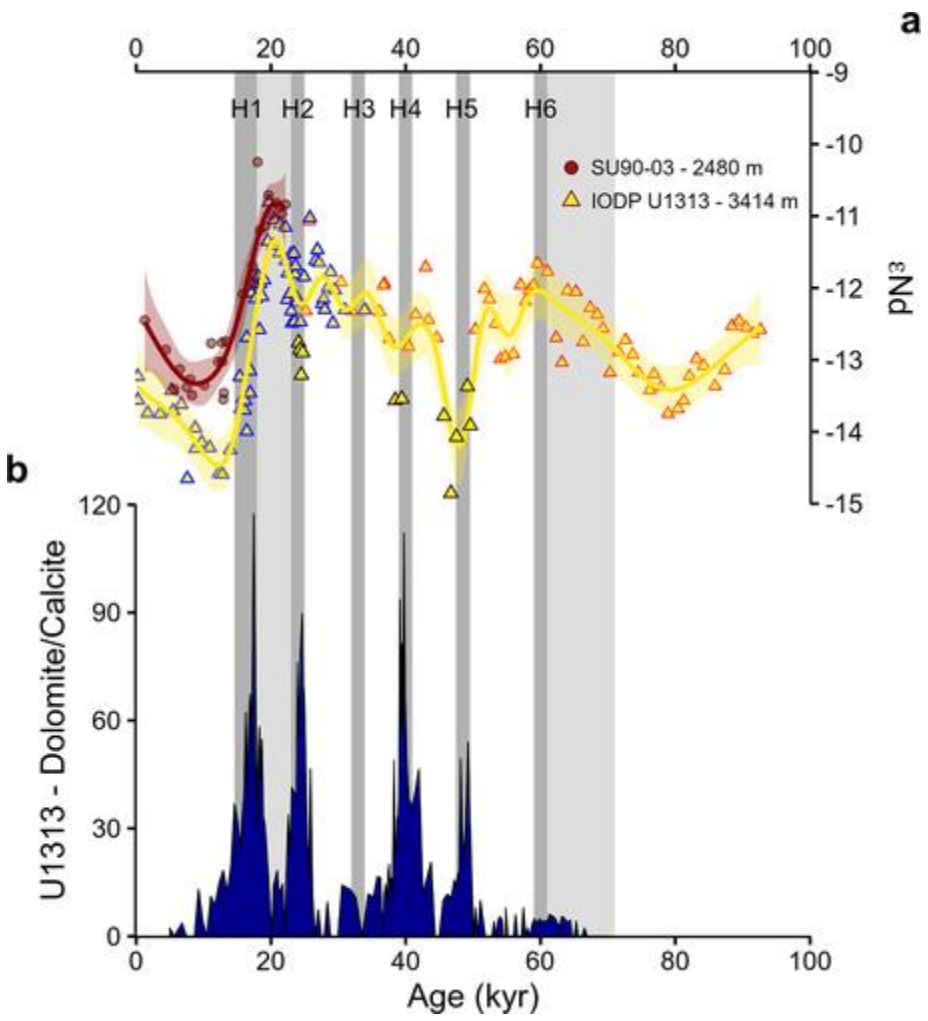

Figure 2. (a) Composite of all published (blue borders, Lang et al., 2016; Lippold et al., 2016; Pöppelmeier et al., 2018) and new εNd data of site U1313 in comparison to εNd data from SU90-03 (Howe, Piotrowski, Noble, et al., 2016) about 1,000 m shallower than U1313 (Figure 1). U1313 data with black borders reflect samples affected by in situ alterations caused by detrital carbonates during major Heinrich events. (b) dolomite/calcite ratios, which only extend back to 70 kyr BP (Naafs et al., 2013).

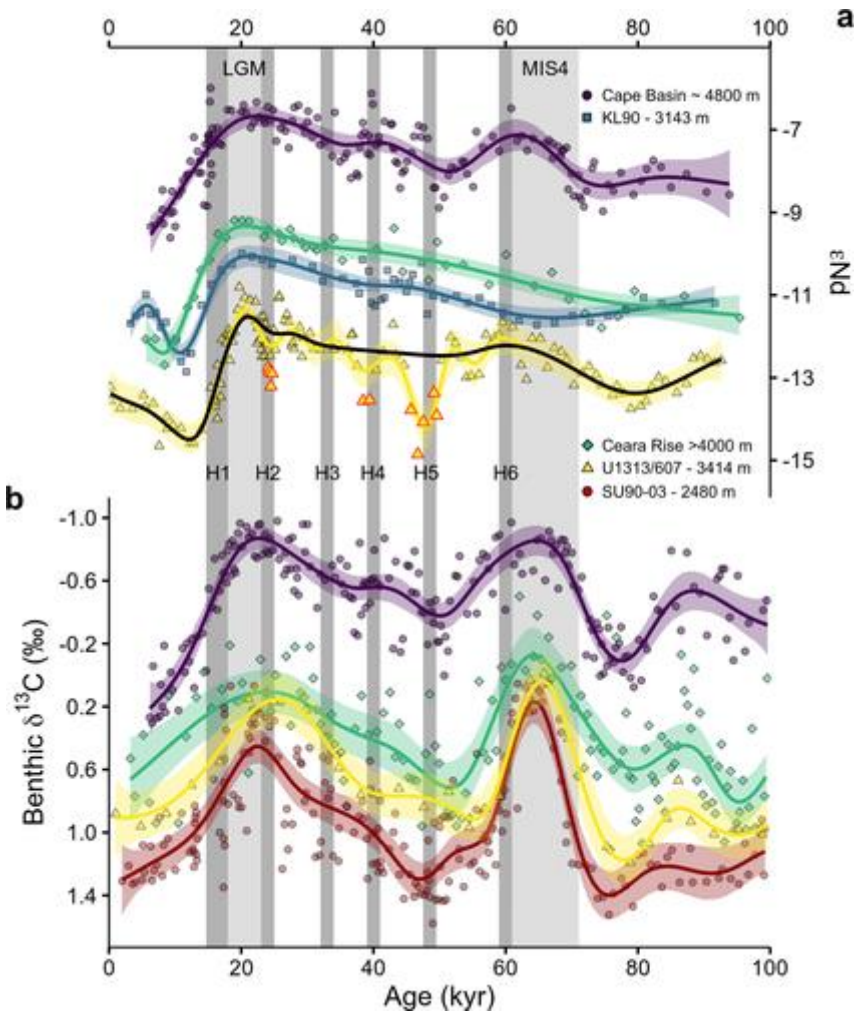

Figure 3. (a) Nd isotope records from the deep Atlantic covering the past 100 kyr. The Cape Basin record is a composite of sites RC11-83 (Piotrowski et al., 2004) and TNO57-21 (Piotrowski et al., 2005). Site U1313 data (past 35 kyr: Lang et al., 2016; Lippold et al., 2016; Pöppelmeier et al., 2018) are complemented by new data back to ~95 kyr BP. Data of ODP 929 and M45/5 KL90 are from Howe and Piotrowski (2017) and Pöppelmeier, Frank et al. (2020), respectively. U1313 data with red borders were excluded for the black line fit due to in situ alterations by detrital carbonate during major Heinrich events. (b) Bottom water stable carbon isotope data ($\delta^{13}C$) of the Cape Basin (TNO57-21, Charles et al., 1996), Ceara Rise (EW9209-1, 4,056 m water depth, proximal to ODP 929, Curry & Oppo, 1997; Figure S3), DSDP 607 (Ruddiman et al., 1989, with refined age model cf. Figure S4), and SU90-03 (Chapman et al., 2000). Lines with error bands (95% confidence interval) represent fits with a generalized additive model.

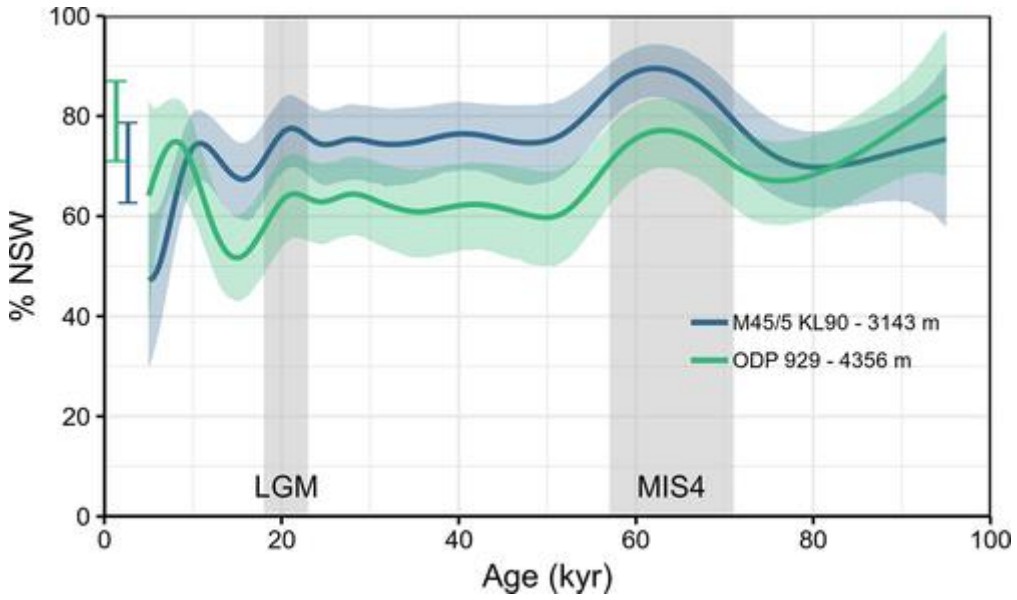

Figure 4. Proportions of northern sourced water (NSW) at sites KL90 (Pöppelmeier, Frank, et al., 2020) and ODP 929 (Howe & Piotrowski, 2017) derived from a binary mixing model assuming U1313 and the Cape Basin composite as northern and southern end-members, respectively. Uncertainties are propagated with a Monte-Carlo approach from the confidence intervals of the end-member records as well as KL90/ODP 929. The uncertainty of the Nd concentration end-members are estimated to ±10% and are also incorporated in the Monte-Carlo error propagation. Modern %NSW based on conservative water mass properties (Jenkins et al., 2015; Pöppelmeier, Blaser, et al., 2020) are marked on the left.